Understanding the p-doping of spiroOMeTAD by tris(pentafluorophenyl)borane

Parth Raval, Margot Dhennin, Herve Vezin, Tomasz Pawlak, Pascal Roussel, Thuc-Quyen Nguyen, Manjunatha Reddy

Understanding the p-doping of spiro-OMeTAD by tris(pentafluorophenyl)borane

Parth Raval,[1] Margot Dhennin,[1] Hervé Vezin,[2] Tomasz Pawlak,[3] Pascal Roussel,[1] Thuc-Quyen Nguyen,[4] and G. N. Manjunatha Reddy[1*]

[1]*University of Lille, CNRS, Centrale Lille Institut, Univ. Artois, UMR 8181−UCCS− Unité de Catalyse et Chimie du Solide, F-59000, Lille, France*

[2] *University of Lille, CNRS UMR8516, LASIRE, F-59000, Lille, France*

[3]*Centre of Molecular and Macromolecular Studies, Polish Academy of Sciences, Sienkiewicza 112, Lodz 90-363, Poland*

[4] *Center for Polymers and Organic Solids, University of California Santa Barbara (UCSB), Santa Barbara, California 93106, USA*

E-mail: gnm.reddy@univ-lille.fr

Keywords: *hole transport, charge transfer, mobility, doping, organic semiconductors, solar cells, solid-state NMR, NMR crystallography, EPR*

Highlights

- Miscibility and intermolecular interactions in p-type doped spiro-OMeTAD hole transporter by tris(pentafluorophenyl)borane are elucidated through a combination of characterization techniques.
- Upon adding BCF to spiro-OMeTAD, different ionic species and active radicals are formed.
- Solid-state 2D NMR spectroscopy combined with crystallography modelling is a powerful tool to probe changes in packing interactions, and the 2D EPR techniques resolve the hyperfine structure of molecularly doped organic semiconductors.

Abstract

The solid-state organization of hole and electron transporting layers plays an important role in governing the performance and stability of emerging optoelectronic devices such as perovskite solar cells (PSCs). The molecular organic semiconductor (OSC) 2,2″,7,7″-tetrakis[N,N-di(4-methoxyphenyl)amino]-9,9′-spirobifluorene (spiro-OMeTAD) is a promising hole-transporting material (HTM) for PSCs, which is p-doped by molecular dopants to augment the charge carrier mobility. Here, the p-type doping of spiro-OMeTAD by tris(pentafluorophenyl)borane (BCF) is investigated by a combination of techniques including optical spectroscopy, X-ray diffraction, Fourier transform infrared (FTIR), solid-state (ss)NMR, and electron paramagnetic resonance (EPR) spectroscopy. BCF molecules interact with traces of water molecules to form BCF-water complexes. Optical spectroscopy analysis suggests that the BCF-water complexes oxidize spiro-OMeTAD molecules and p-type doping spiro-OMeTAD molecules. The different distributions of BCF and BCF-water molecules in doped spiro-OMeTAD are characterized by FTIR and ^{11}B NMR spectroscopy. An NMR crystallography approach which combines two-dimensional (2D) ssNMR and crystallography modelling is employed to unravel the packing interactions in spiro-OMeTAD, and this analysis is extended to probe the morphological and structural changes in spiro-OMeTAD:BCF blends. The hyperfine interactions are characterized by 2D hyperfine sub-level correlation (HYSCORE) spectroscopy. In this way, insight into the complex spiro-OMeTAD:BCF blend morphology is obtained and compared for different dopant concentrations. Molecular-level analysis of doped HTMs enabled by this study has much wider relevance for further investigation, for example, chemical design and interfacial engineering of p-type doped HTMs for stable and efficient hybrid perovskite photovoltaics.

TOC graphic

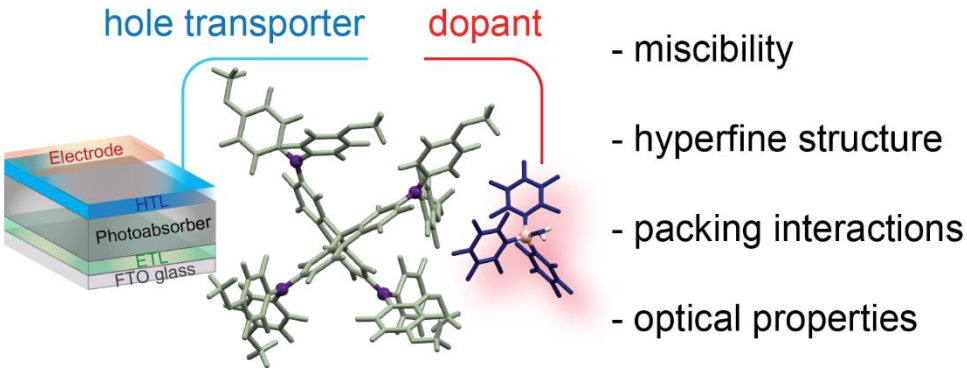

Introduction

Solution-processed semiconductors such as organic semiconductors (OSCs) and metal halide perovskites (MHPs) are among the systems of fundamental and technological interest for a range of energy and optoelectronic applications including solar cells, photocatalysis, sensors, light-emission, and display technologies.[1–5] In this context, it is vitally important to engineer the nanoscale compositions and structures of contact layers, photoabsorber layers and interfaces between them in order to develop stable and efficient optoelectronic devices. For example, the reactive interfaces between photoabsorbing layers and the charge-transporting materials play a pivotal role in governing the overall performance and environmental stability of perovskite solar cells (PSCs).[6–13] The hand-in-hand progress on the molecular design of OSC-based hole-transporting materials (HTMs) and MHP-based photoabsorbers is synergistically attaining high performance and stable optoelectronic devices. [14–17]

The formal single-junction perovskite solar cells commonly employ mesoporous titania (TiO_2) as an electron transporter and a small-molecule OSC (spiro-OMeTAD) [2,2′,7,7′-tetrakis(N,N-di-p-methoxyphenyl-amine)9,9′-spirobifluorene] as a hole transporting layer.[13,14,18] Since its replacement as a solid analogue to the liquid electrolyte-based HTMs, spiro-OMeTAD and its derivatives have enabled the major advancements in the PSCs with power conversion efficiencies exceeding 24% in single-junction cells.[14–17] Although solution-processed spiro-OMeTAD thin

films exhibit relatively low conductivity, chemical doping and additive engineering strategies were sought to enhance the conductivity of spiro-based HTMs. For example, crystallization strategies of spiro-OMeTAD molecules have been employed to improve the charge carrier mobilities in field-effect transistor devices, and molecularly p-doped spiro-OMeTAD HTMs enabled the development of high-efficiency PSCs and dye-sensitized solar cells DSCs.[19–23] Interfacial and additive engineering of charge transport layers as well as photoabsorber layers have been used to improve the performance and stability of the perovskite-based solar cells.[24–26] In addition, chemical doping of HTMs using small molecule dopants such as 2,3,5,6-tetrafluoro-7,7,8,8-tetracyanoquinodimethane (F4TCNQ), bis(trifluoromethane) sulfonamide lithium salt (LiTFSI), benzoyl peroxide and 4-tert-butylpyridine (TBP) has been used to augment the charge carrier properties.[14,27–29] Additive engineering and doping strategies facilitate better charge transport, suppresses the recombination rates, and inhibit the formation of trap states.[28,29] Although doping provides numerous advantages, some strategies lead to undesired chemical transformations and degradation reactions. For example, Li-TFSI dopant oxidizes spiro-OMeTAD in the presence of oxygen, light, or thermal excitation,[8,30,31] leading to degradation reactions that impart hysteresis in device reproducibility, stability, and performance.[30–35] Molecular doping strategies based on small molecules such as tris(pentafluorophenyl)borane (BCF), dimethylsulphoxide (DMSO)/HBr adducts, acid additives, and organic metal salts have been used to improve the conductivity, stability, and performance of spiro-OMeTAD based HTMs.[7,36–38] The strong electron-accepting ability, excellent solubility in common organic solvents, and cost-effectiveness are among the factors that make BCF a suitable dopant for OSCs. In addition, BCF molecules interact with traces of water molecules to form Brønsted acid BCF-water complexes which have been shown to p-dope a wide range of Lewis basic π–conjugated molecules. The optoelectronic properties and bandgap of OSCs can be effectively tuned by adding BCF molecules to OSCs.[39–43] Although BCF-doped OSCs have been extensively used in organic light-emitting diodes (OLEDs),[40] photodetectors (OPDs), and field-effect transistors (OFETs),[39] a few recent studies demonstrate the potential of BCF as a p-type dopant for HTMs and as molecular passivator in perovskite-based photovoltaics.[36,44,45] The different mechanisms through which doping of OSCs occurs in the presence of BCF molecules have been discussed in great detail in the literature using experimental results and theoretical calculations.[19,46–49] The p-type doping by BCF molecules occurs either by forming a charge-transfer supramolecular complex between BCF and OSC,[46] or by forming an

acid-base complex when Lewis basic OSC shares its lone electron pair with the B atom of BCF, resulting in a partial charge transfer between the donor and acceptor species.[47] Alternative mechanisms including the ground-state integer charge-transfer models have also been proposed, whereby an electron transfer from OSC to BCF yields a positively charged OSC cation and a negatively charged BCF anion.[41,50] A molecular-level understanding of different doping mechanisms necessitates an accurate characterization of OSC-dopant intermolecular interactions at different length scales.

Owing to the compositional and structural heterogeneity associated with the doped OSCs, molecular-level insight into the dopant-OSC intermolecular interactions is often difficult to obtain. Recently, several experimental and theoretical investigations have been carried out to understand the different doping mechanisms in OSCs induced by the addition of small molecules.[19,37,38,47–49,51–53] The addition of dopant molecules causes changes to the molecular self-assembly and morphological features that are difficult to resolve by X-ray scattering and microscopy techniques. While electroanalytical and UV-visible spectroscopy techniques provide information on the macroscopic changes such as conductivity and optical absorption, these techniques offer limited insights into dopant-OSC miscibility, intermolecular interactions, and mechanistic details of the molecular doping process. Therefore, a precise understanding of the structure-property relationship in doped OSCs necessitates the characterization using atomic-level probes such as solid-state (ss)NMR spectroscopy and EPR spectroscopy, which do not rely on long-range order and are sensitive to the short-range interactions in both crystalline and amorphous regions of OSC-dopant blends. In particular, magic-angle spinning (MAS) NMR techniques have been increasingly applied to gain molecular-level insight into the microstructures, order, and disorder in organic semiconductors and hybrid perovskites.[18,54–59] A recent study employs combined 2D ssNMR and EPR techniques to resolve specific intermolecular interactions and the electron-nuclear hyperfine structure of the BCF-doped conjugated polymer.[60]

Here we investigate the optical and morphological properties of undoped and p-doped spiro-OMeTAD with a Lewis acid BCF (Figure 1), and examine the local structures and interactions between molecular dopant and host organic semiconductor using magnetic resonance spectroscopy and crystallography modelling techniques. While XRD and FTIR analysis provided limited structural insights into the intermolecular interactions between spiro-OMeTAD and BCF,

the ^{11}B MAS NMR spectroscopy distinguished different boron sites in the BCF-doped spiro-OMeTAD compared to the pristine BCF, indicating that the BCF molecules interact with spiro-OMeTAD molecules. The morphological features of undoped and doped thin films are characterized by 2D ssNMR and EPR spectroscopy techniques. An NMR crystallography approach (which combines ssNMR and computational modelling) has been employed to unravel the self-assembly and packing interactions in pristine spiro-OMeTAD. We extended this approach to identify and distinguish the morphological and local structural changes in undoped and BCF-doped spiro-OMeTAD molecules. By combining several characterization techniques and theoretical modelling, we develop a framework to gain molecular-level insight into the impact of dopant molecules on the structures and properties of the host OSCs, which appears to be a general approach for the study of molecularly doped organic semiconductors.

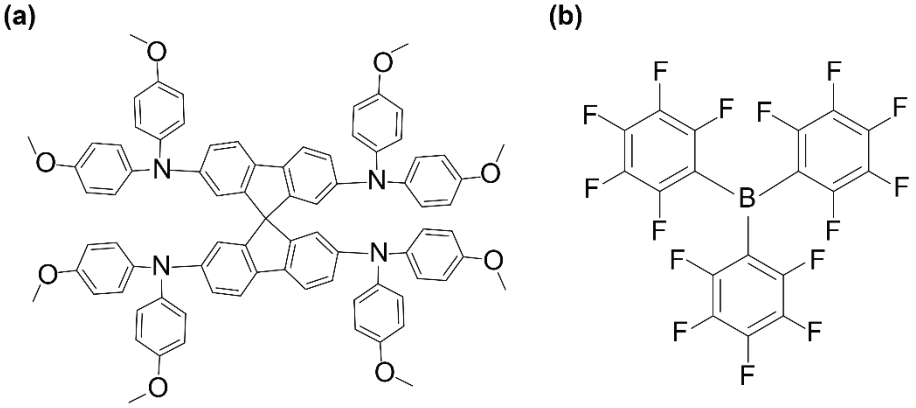

Figure 1. Chemical structures of (a) spiro-OMeTAD and (b) tris(pentafluorophenyl)borane (BCF).

Experimental

Materials and methods. The solvents, spiro-OMeTAD, and BCF were purchased from Sigma Aldrich in a purity greater than 98% and used as received. All solvents were purchased dry, and molecular sieves were added to the solvents. The BCF was stored and handled in a nitrogen atmosphere glovebox to prevent water contamination. However, BCF is hygroscopic and interacts with traces of water molecules (present in solvents during the film deposition, and upon exposure to ambient moisture during the sample preparation to ssNMR experiments, i.e., scratching of thin films from the glass substrates and packing NMR rotors), which leads to the formation of BCF-

water complexes. For solution-state optical spectroscopy measurements, separate solutions of spiro-OMeTAD and BCF were prepared (0.01 mmol/L) using chlorobenzene as the solvent. These solutions were placed on a vortex mixer for 10 minutes at room temperature to ensure the complete dissolution of OSC and dopant molecules. Stoichiometric amounts of BCF solution were added to the spiro-OMeTAD solution to prepare spiro-OMeTAD:BCF blends with 1:0.1, 1:0.2, 1:0.5, 1:1, 1:2, and 1:4 molar ratios, and the resultant solutions were homogenized with a vortex agitator for 10 minutes at room temperature.

UV-visible absorption spectroscopy. UV-visible absorption spectra were measured using Perkin Elmer Lambda 650 spectrophotometer. All experiments were carried out at room temperature. The spectra were acquired for the liquid samples (0.01 mmol.L^{-1}) prepared as mentioned in the above section with a resolution of 1 nm.

X-ray diffraction. A Rigaku Smartlab diffractometer equipped with a copper rotated anode operated at 45kV and 200mA was used to record patterns of pristine, undoped, and doped spiro-OMeTAD thin films drop cast on ITO-coated glass substrates. Diffractograms were acquired in parallel beam configuration between 5 and 50° with a 0.01° step on a Rigaku HyPix3000 detector.

Attenuated total reflectance Fourier transform infrared (ATR-FTIR) spectroscopy. Perkin Elmer FTIR Spectrum two UATR spectrometer was used to acquire IR spectra of thin films of neat and doped spiro-OMeTAD, which were obtained by scratching the drop-casted film. The spectra were acquired with 20 scans and spectral resolutions of 4 cm^{-1}.

Solid-state NMR spectroscopy. Samples for the ssNMR experiments were obtained by drop-casting the solutions (10 mg/mL) containing pristine spiro-OMeTAD, BCF, spiro-OMeTAD: BCF (1:0.25, 1:0.5,1:1, 1:4 molar ratios) on ITO-coated glass substrates, and annealed at 70 °C for 20 minutes. These thin films were scratched from the glass substrates to collect enough material (~10 mg) into a glass vial. The samples were separately packed into either 1.3 mm or 2.5 mm (outer diameter) cylindrical zirconia rotors and fitted with Vespel® caps. All 1D ^{1}H, ^{13}C, ^{11}B, and 2D ^{1}H-^{1}H MAS NMR experiments of pristine spiro-OMeTAD, BCF, and spiro-OMeTAD:BCF blends (1:1 and 1:4 molar ratio) were carried out on a Bruker AVANCE NEO (18.8 T, Larmor frequencies of ^{1}H, ^{13}C, and ^{11}B were 800.1 MHz, 201.2 MHz, and 256.7 MHz, respectively) spectrometer with 1.3 mm H-X probe head operating at room temperature. Unless otherwise mentioned, the magic-

angle spinning (MAS) frequency was 50 kHz for all experiments. The ^{1}H and ^{13}C chemical shifts were calibrated with respect to neat TMS using adamantane as an external reference (higher ppm ^{13}C resonance, 38.5 ppm, and the ^{1}H resonance, 1.85 ppm), and the ^{11}B NMR shifts were referenced using an external standard $NaBH_4$ (^{11}B peak at –42.06 ppm), which is calibrated to $BF_3.OEt_2$ (^{11}B, 0 ppm) in $CDCl_3$. The ^{19}F NMR spectra were calibrated with respect to ^{19}F chemical shifts of neat $CFCl_3$ (^{19}F, 0 ppm) as an external reference.[61]

All 1D ^{1}H MAS NMR experiments were carried out by co-adding 32 transients using a relaxation delay of 4 seconds. The 1D ^{11}B MAS NMR spectrum of neat BCF material was acquired by co-adding 256 transients, and the spectra of spiro-OMeTAD:BCF blends were acquired with 2048 co-added transients using a repetition delay of 2 seconds. All the 1D ^{19}F MAS NMR experiments were carried out at 9.4 T (^{19}F Larmor frequency = 376.5 MHz) with 30 kHz MAS using a 2.5 mm H-X probehead, and each spectrum was acquired by co-adding 32 transients with a relaxation delay of 3 seconds. For undoped and doped Spiro-OMeTAD materials, the 1D $^{1}H \rightarrow {}^{13}C$ CP-MAS spectra were acquired with 2048 and 5120 co-added transients and CP contact times of 2 ms and 4 ms, respectively. The 2D ^{1}H-^{1}H DQ-SQ spectra of pristine and doped spiro-OMeTAD were acquired with 96 t_1 increments, each with 16 co-added transients, using a Back-to-Back (BaBa) sequence at fast MAS.[62,63] The ^{1}H detected 2D ^{1}H-^{13}C HETCOR spectra of pure spiro-OMeTAD were acquired with 256 t_1 increments, each with co-addition of 24 transients, with short (100 μs) and long (3 ms) CP contact times.

Quantum mechanical calculations. Input files for periodic DFT calculations were prepared by taking molecular coordinates from previously published crystal structures of spiro-OMeTAD (The Cambridge Crystallography Data Centre (CCDC) code: 1475944),[23], and BCF-water complexes (CCDC codes: 10429, and 1861707).[64,65] The pristine spiro-OMeTAD molecule is a 1292-electron system, and the BCF-water complex is a 556-electron system. For spiro-OMeTAD, we first performed a convergence test. In this test, we carried out a series of calculations by varying cut-off energy and monitored the convergence of the total energy of the molecular system in its irreducible representation (i.e., an asymmetric unit cell). The geometry optimization was performed using periodic DFT calculations, and the gauge including the projected augmented wave (GIPAW) method as described by Pickard and Mauri was used for the computation of NMR nuclear shieldings.[66] All DFT calculations were performed using the CASTEP 19.11 code.[67] Each

SCF loop was performed until the energy was converged within 3.67×10^{-8} Hartrees. For all calculations, the generalized density approximation DFT functional PBE with the Tkatchenko-Scheffler (TS) dispersion correction scheme (DFT-D method) was applied, and the maximum plane wave cut-off energy was 29.4 Hartrees using an ultrasoft pseudopotential.[68–70] In all cases, the optimization algorithm was BFSG, and the Monkhorst−Pack grid of minimum sample spacing $0.07 \times 2\pi$ Å^{-1} was used to sample the Brillouin zone.[71,72] During the calculations, the positions of the atoms were varied within the unit cell until the average forces, energies, and displacements were converged to below 3.6749×10^{-7} Hartree/Å, 0.0011025 Hartrees, and 0.001 Å, respectively. The crystallographic information (CIF) and magnetic resonance shielding (magres) files are visualized using Mercury4.0 and Magresview tools.[73] The 2D spectra of calculated chemical shifts were generated using the Magresview package (available at www.ccpnc.ac.uk).

Solid-state EPR spectroscopy. All 1D X-band continuous-wave length (CW) EPR spectra were acquired with a Bruker ELEXYS E500 operating at cryogenic temperatures. For EPR pulses, the amplitude modulation and microwave power were 0.5 G and 1 mW, respectively. Relaxation times were measured on a Bruker ELEXYS E580 at 10 K using a 1D Hahn-echo sequence for T_2 (transverse relaxation) and inversion recovery for T_1 (longitudinal relaxation) measurements. For the homogenous EPR spectral lineshape, T_2 was measured from FID decay as T_1 was measured using FID inversion recovery sequence. The $\pi/2$ and π pulses were 24 and 50 ns, respectively. For pulsed 2D hyperfine sublevel correlation spectroscopy (HYSCORE) experiments, a four-pulse sequence $(\pi/2)$-τ–$(\pi/2)$- t_1–(π)-t_2–$(\pi/2)$–detection(echo) sequence was used. The pulse lengths of $\pi/2$ and π pulses of 28 ns and 52 ns, and the delay τ = 300 ns were chosen to remove the strong FID signal due to the homogenous part of the EPR signal in order to prevent blind spot effects. The 2D spectra were acquired with 256×256 time-domain (t) data points to build t_1 and t_2 dimensions. The unmodulated part of the echo was removed by second-order polynomial subtraction. Finally, 2D Fourier transformation and a Hamming apodization window function were applied to obtain the HYSCORE spectra.

Results and discussion

To understand the impact of addition of dopant molecules on the optical properties of the host organic semiconductor, we carried out absorption measurements and analysis. Figure 2 compares the optical absorption spectra of undoped and doped spiro-OMeTAD (450-800 nm) as a function of the BCF dopant concertation in chlorobenzene. Full optical absorption spectra (275-800 nm) are presented in Supporting Information (Figure S1). Upon the addition of BCF molecules to the spiro-OMeTAD solution, absorption peaks in the 490-530 nm range have emerged. Intensities of these peaks increase as the BCF concentration increases from 0.1 to 1 molar equivalents. These optical absorption features are characteristic of the oxidized spiro-OMeTAD^{+} molecules because spiro-OMeTAD molecules are well known to undergo redox-type reactions in the presence of dopants.[21,36] This is consistent with the previous studies that showed the addition of p-dopants led to such changes in the optical absorption and bandgap of HTMs.[36,74] In addition, broad and weak intensity features appeared at 650 and 750 nm for spiro-OMeTAD:BCF (1:2 molar ratio) molecules (Figure S1), which can be attributable to BCF anion and spiro-OMeTAD^{+} cation species. However, the peaks characteristic of the Lewis acid-base spiro-OMeTAD:BCF adduct are not observed in the UV−vis absorption spectra, if present, such adduct would have led to the red-shift in the optical absorption peak.[47] These results suggest that the BCF molecules are closely associated with spiro-OMeTAD backbone moieties rather than forming the adduct. The ground-state electron transfer from the spiro-OMeTAD to the BCF-water complex is corroborated by the increased intensity of the peak at ~530 nm.[50] Although the changes in the optical properties indicate that the BCF is closely associated with the spiro-OMeTAD molecules, the molecular level origins that contribute to the changes in optical absorption in doped spiro-OMeTAD molecules are difficult to obtain from UV-Vis spectroscopy alone, which necessitates the structural characterization.

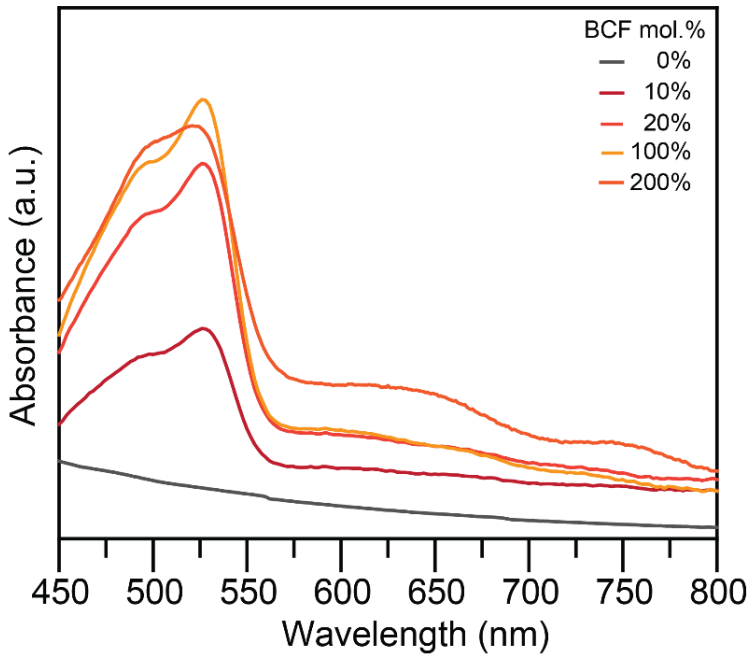

Figure 2. UV-Vis spectra of undoped and BCF-doped spiro-OMeTAD as a function of dopant concentration in chlorobenzene.

Morphological features and local structures of undoped and doped spiro-OMeTAD. A detailed analysis of the morphological features at different length scales is expected to provide insights into the dopant-OSC interactions. Owing to the dilute concentrations of dopant molecules and the inherently heterogenous nature of OSCs-dopants blends, these materials represent a characterization challenge. Figure S3 (Supporting Information) presents the powder XRD patterns of the neat spiro-OMeTAD and spiro-OMeTAD:BCF blends (1:1 and 1:4 molar ratios) drop cast on ITO-coated glass substrate. BCF-doped spiro-OMeTAD exhibited a broad distribution of scattered intensities centered at ~18°, corresponding to a *d*-spacing value of roughly 0.45 nm, which could be attributed to the weak π–π stacking interactions between BCF and spiro-OMeTAD molecules. This subtle change in the long-range order, as observed by XRD, indicates structural changes in the thin film. Given the heterogeneous nature of OSCs, obtaining a deeper molecular-level understanding using long-range probes such as X-ray diffraction is challenging; atomic-level probes are required to obtain information on the changes in local structures upon the addition of BCF molecules to the spiro-OMeTAD.

To gain further insight into the impact of BCF addition to spiro-OMeTAD, FT-IR spectra of drop cast films were acquired and compared for the neat and doped spiro-OMeTAD molecules. Fourier transform infrared (FTIR) spectroscopy can be used to identify the changes in the local environments of chemical bonds by analyzing absorption bands. Solid-state FT-IR spectra of undoped and doped spiro-OMeTAD are presented in Figure 3. The vibrational bands corresponding to B-C stretching are observed in the 900-1000 cm^{-1} range - intensities of which are increased upon addition of BCF molecules - indicating the presence of BCF molecules in the spiro-OMeTAD:BCF blend films.[75] Stretching frequencies in the 1000-1400 cm^{-1} range are attributable to C-O and C-N bonds in spiro-OMeTAD, and C-F bonds in BCF molecules,[76–78] and peaks in the 1400-1600 cm^{-1} range are ascribed to the stretching frequencies of aromatic C=C bonds phenyl and bifluorene moieties of spiro-OMeTAD and fluorinated phenyl rings in BCF molecules.[79] The most notable of all is the vibrational band at 1562 cm^{-1} associated with the B-OH stretching frequency, which is further corroborated by the strong and broad vibrational band centered at ~3200 cm^{-1}.[80] In addition, the vibrational band at ~3200 cm^{-1} can also be ascribed to N-H stretching frequency, which corroborates the presence of different ionic species such as spiro-OMeTAD-H^+ cations and BCF-OH^- anions. The subtle changes in the vibrational bands in the 2800-3100 cm^{-1} range are attributable to the changes in local C-H bonding environments of spiro-OMeTAD upon the addition of BCF molecules. Analysis of FT-IR spectra indicates the presence of different dopant species, which corroborate the optical spectroscopy measurements and analysis.

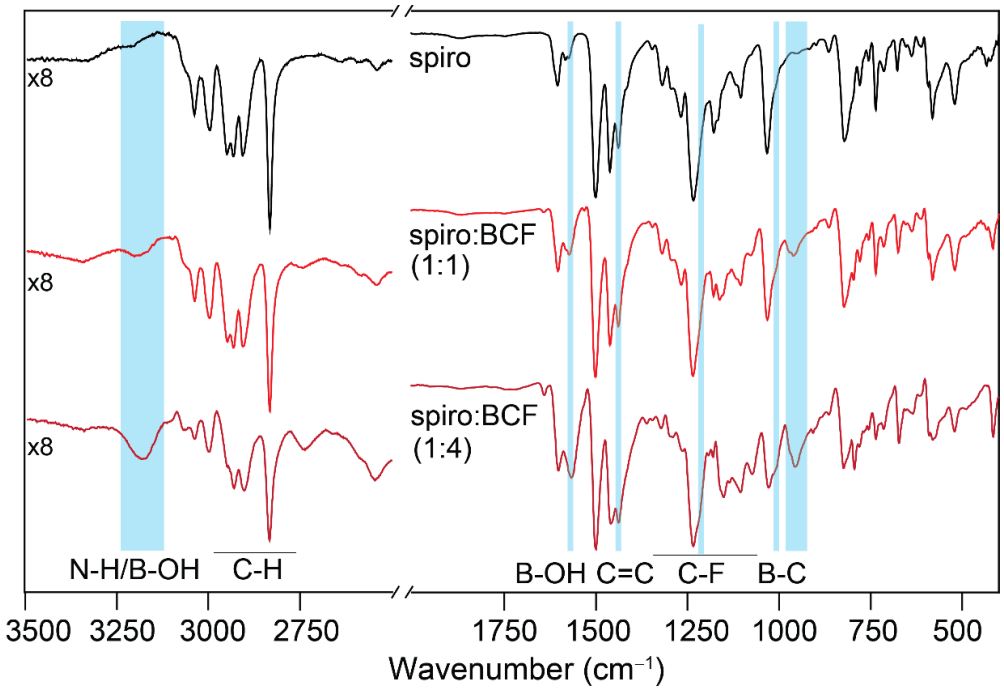

Figure 3. Solid-state attenuated total reflection FT-IR spectra of undoped and doped spiro-OMeTAD thin films acquired at room temperature.

Insight into local structures by solid-state NMR spectroscopy. To understand the local compositions, structures, and intermolecular interactions in neat spiro-OMeTAD and BCF-doped spiro-OMeTAD films, solid-state (ss)NMR spectra of neat compounds and blends were acquired and compared. Multinuclear ssNMR spectroscopy has been increasingly applied to gain insight into the local structures in organic semiconductors and their blends.[54,81–83] Of particular note, 2D NMR correlation spectra acquired at high fields with fast magic-angle spinning (MAS) techniques provide enhanced resolution to probe inter- and intramolecular interactions in both ordered and disordered regions of the complex OSC materials.[54,58,84–88] Here, we examine ^{11}B, ^{1}H, and ^{13}C chemical shifts (Figure 4) and through-space proximities between these nuclei, facilitating the structure-based understanding of neat spiro-OMeTAD and spiro-OMeTAD:BCF blends. For pristine BCF, the 1D ^{11}B MAS NMR spectrum (Figure 4a) displays two distinct features, which can be attributed to tri-coordinated boron atoms in BCF and tetra-coordinated boron atoms in BCF-water complexes. For the spiro-OMeTAD:BCF blend (1:1 molar ratio), a relatively narrow ^{11}B NMR signal centered at −5 ppm is due to tetrahedral boron atoms in BCF anions, and the weak intensity signals centered at 17 and 23 ppm are attributable to distinct BCF-water complexes.

Likewise, spiro-OMeTAD:BCF blends with 1:0.25 and 1:0.5 molar ratios exhibited a strong intensity ^{11}B NMR peak at −5 ppm (Supporting Information, Figure S3), indicating the formation of tetracoordinated borate anions, and the signals in 0-20 ppm range (for 1:0.5 molar ratio blend) are due to the formation of distinct BCF-water complexes. These latter signals appeared at much higher intensity in the ^{11}B MAS NMR spectrum of spiro-OMeTAD:BCF blend (1:4 molar ratio), indicating that the BCF-water complexes are formed when a higher concentration of BCF (> 1 molar equivalents) is added to spiro-OMeTAD. Periodic density-functional theory (DFT) calculations of BCF-H_2O and BCF-$H_2O.2H_2O$ complexes further support these assignments, whereby ~5 ppm difference in the calculated isotropic ^{11}B chemical shifts and ~0.6 MHz difference in the calculated quadrupolar coupling constants between these two BCF-water complexes are observed. The ^{11}B NMR results are corroborated by the analysis of ^{1}H, ^{19}F and ^{13}C NMR spectra.

In the ^{1}H NMR spectrum of neat spiro-OMeTAD (Figure 4b), partially resolved signals at 2-5 ppm are due to methoxy groups, and the peaks at 5-8 ppm are associated with the phenyl and fluorene protons. The addition of BCF to spiro-OMeTAD causes signal broadening and intensity losses. The peak integrals associated with aromatic protons reduce to 52% (spiro-OMeTAD:BCF, 1:1) and 31% (spiro-OMeTAD: BCF, 1:1), compared to the aromatic peak intensity of pristine spiro-OMeTAD (100%). The methoxy ^{1}H signals exhibited 37% and 70% intensity losses for spiro-OMeTAD: BCF blends (1:1 and 1:4 molar ratios), further indicating the formation of radical cations and other forms of paramagnetic species in the doped material, as confirmed by EPR analysis discussed below. Additionally, the 1D ^{1}H NMR spectrum of spiro-OMeTAD:BCF (1:0.25 and 1:0.5 molar ratio) blends shown in Supporting Information Figure S4 exhibited similar peak broadening. For the neat BCF, ^{19}F NMR signals between −134 and −141 ppm correspond to the *ortho*-fluorine sites, and the peaks between −160 and −171 ppm are due to *meta* and *para* fluorine sites of pentafluorophenyl rings.[47] The narrow ^{19}F signals indicate the well-ordered pentafluorophenyl rings in BCF molecules. By comparison, the spiro-OMeTAD:BCF blends with 1:0.25, 1:0.5, and 1:1 molar ratios (Figures 4c, S5) exhibit broad signals that indicate the different local chemical environments of fluorinated phenyl groups, which can be further corroborated by the 1D ^{1}H and ^{13}C NMR analyses that showed similar peak broadening due to the presence of paramagnetic species and local heterogeneities in the local chemical environments of spiro and BCF molecules. Upon further increasing the BCF concentration to 4 molar equivalents, both

narrow and broad ^{19}F spectral features are observed, which are hypothesized to originate from the different distribution of dopant molecules, including well-intermixed BCF molecules and phase-separated BCF and BCF-water complexes (that are identical to the neat BCF molecules) in the blend.

By analyzing $^{1}H \rightarrow ^{13}C$ cross-polarization (CP)-MAS NMR spectra of spiro-OMeTAD acquired with different CP contact times, the directly bonded and through-space dipolar coupled C-H moieties can be identified and distinguished (Figure 4d). Well-resolved ^{13}C signals indicate the high degree of structural order in neat spiro-OMeTAD material. The methoxy ^{13}C signals appeared at 53-56 ppm (orange dots), and the signal at 66 ppm is attributed to the quaternary carbon atom at the bridging position (pink dot) of central bifluorene moiety. In the aromatic region, the ^{13}C signals at 107-133 ppm are assigned to the directly bonded C-H moieties in phenyl and bifluorene moiety (gray and cyan dots), and the signals in the range of 135-160 ppm are ascribed to the quaternary carbon atoms (green, blue, red and burgundy dots), which are further corroborated by periodic DFT calculated NMR chemical shifts of crystalline spiro-OMeTAD using the GIPAW approach, as discussed below. By comparison, the $^{1}H \rightarrow ^{13}C$ CP-MAS NMR spectrum of spiro-OMeTAD: BCF (1:4) blend exhibited relatively broad signals for both methoxy and aromatic regions, consistently with the ^{1}H NMR peak broadening, due to the interpenetration of BCF molecules that disrupt the self-assembly and packing interactions in spiro-OMeTAD molecules as well as the formation active radical species. Although local ^{1}H and ^{13}C chemical shifts characterized by conventional 1D MAS NMR spectra provide information on the local bonding environments, these measurements do not provide information on the intermolecular interactions between BCF and spiro-OMeTAD molecules.

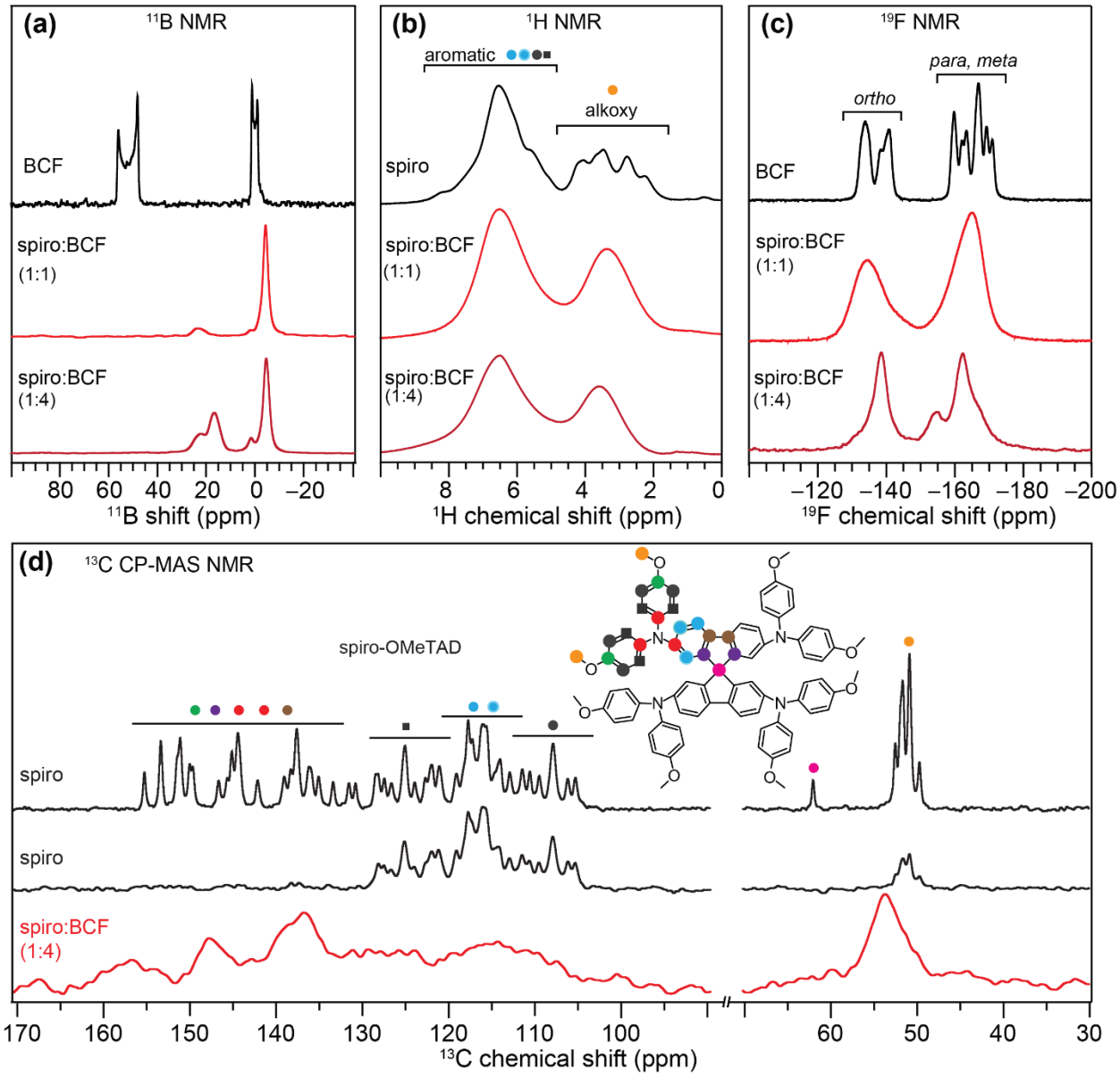

Figure 4. Solid-state (a) ^{11}B MAS NMR spectra of neat BCF and spiro-OMeTAD:BCF blends (b) ^{1}H MAS (c) ^{19}F MAS and (d) ^{13}C CP-MAS NMR spectra of neat spiro-OMeTAD (CP contact time of 2 ms – top and 60 μs – middle) and spiro-OMeTAD:BCF blends with dopant concentrations indicated in the insets. The peaks are color-coded as depicted in the schematic structure in (d).

Beyond the resolution capabilities of 1D MAS NMR, we employed 2D ^{1}H-^{13}C heteronuclear correlation and ^{1}H-^{1}H Double-Quantum–Single-Quantum (DQ-SQ) correlation

NMR spectroscopy to analyze OSC-dopant inter- and intramolecular interactions. In these experiments, 2D peaks are detected for the through-space and dipolar coupled ^{1}H-^{13}C and ^{1}H-^{1}H pairs at sub-nanometer distances. Notably, calculated ^{1}H and ^{13}C chemical shifts using the GIPAW DFT-D approach facilitate the analysis of 2D NMR spectra of neat spiro-OMeTAD molecules, from which the information on molecular self-assembly and packing interactions can be deduced. This analysis can be extended to examine the changes in the local structures and packing interactions between spiro-OMeTAD molecules upon doping with BCF molecules, for example, by analyzing and comparing the experimental 2D NMR correlation spectra of undoped and doped spiro-OMeTAD materials. In this way, a combination of modelling and experimental analysis can be used to gain a structural insight into the doped OSC material.

Figure 5 presents 2D ^{1}H-^{13}C HETCOR spectra of neat spiro-OMeTAD acquired with short and long CP contact times. Specific packing interactions that contribute to the 2D peaks are depicted in Figure 5a. The GIPAW DFT-D calculated ^{1}H and ^{13}C NMR chemical shifts for dipolar coupled ^{1}H-^{13}C pairs are overlaid on the experimental spectra, and the 2D peaks are color-coded as depicted in the schematic structure (Figure 5b, inset). In the 2D HETCOR spectrum acquired with a short CP contact time (100 μs, Figure 5b), the 2D correlation peaks corresponding to the directly bonded ^{13}C-^{1}H spin pairs are observed. For directly-bonded ^{1}H-^{13}C moieties, good agreement between experimental and DFT-calculated 2D peaks is observed, although subtle changes in the ^{1}H chemical shifts (9-10 ppm) are observed. These differences are attributable to the changes in the local packing interactions due to the high degree of conformational flexibility associated with phenyl rings and methoxy groups. The 2D peaks correlating ^{1}H (2.8-4.1 ppm) and ^{13}C signals (53-56 ppm) correspond to C-H moieties within methoxy groups (yellow circle) of spiro-OMeTAD. In the aromatic region, the directly bonded phenyl ^{13}C-^{1}H moieties (grey dot and square) are observed at ^{1}H (5.6-6.4 ppm) and ^{13}C (113-119 ppm) signals and at ^{1}H (6.6 ppm) and ^{13}C (133-135 ppm) signals, and the 2D peaks associated with the fluorene moieties (turquoise dots) of the spiro-OMeTAD core appeared at ^{1}H (5.4-7.5 ppm) and ^{13}C (122-130 ppm) signals. In order to distinguish the 2D speaks originating from the directly bonded ^{13}C-^{1}H moieties from those of through-space dipolar coupled ^{13}C$^{\cdots}$^{1}H moieties, an additional 2D HETCOR spectrum acquired with a long CP contact time has been analyzed and compared. By comparison, the 2D HETCOR spectrum of the same material acquired with a

longer CP contact time (3 ms, Figure 5c) exhibited markedly different correlation peaks, which originate from both inter- and intramolecular dipolar coupled ^{13}C-^{1}H spin pairs at sub-nanometer distances. For all ^{13}C-^{1}H spin pairs within 2.8 Å, the GIPAW DFT-D calculated ^{1}H and ^{13}C chemical shifts are overlaid on the experimental spectra. The inter- and intramolecularly dipolar coupled methoxy ^{13}C (yellow dots) and phenyl ^{1}H sites (grey dot and square) lead to a 2D peak at ^{1}H (6.2-6.6 ppm) and ^{13}C (53-56 ppm) chemical shifts as indicated by the red arrow. The inter- and intramolecular ^{13}C-^{1}H distances associated with these moieties are 3.4 Å and 2.8 Å, as shown in the crystal structure (Figure 5a). The 2D peak at ^{13}C (~55 ppm, pink dot) and the ^{1}H (6-7 ppm, blue dots) is due to the intramolecular through-space interactions between quaternary carbon atom at the bridged position of bifluorene moieties and bifluorene protons. In addition, the inter- and intramolecularly proximate bifluorene quaternary carbon atoms (brown dots) and bifluorene protons give rise to a 2D peak between ^{13}C (135-139 ppm) and ^{1}H (6.5-6.9 ppm), for which the closest inter- and intramodular distances are 3.3 Å and 2.2 Å in the GIPAW DFT-D optimized crystal structure of spiro-OMeTAD. Subsequently, the quaternary phenyl C_{α} (141-144 ppm, red dots) are in close proximity with phenyl and fluorene protons (5.1–7.4 ppm) with the closest inter- and intramolecular C-H distances of 3.4 and 2.2 Å, respectively. The same quaternary fluorene C_{α} (red dot) is closely proximate with the fluorene and phenyl protons resulting in the 2D peaks between ^{13}C (146-150 ppm) and ^{1}H (5.4-7.6 ppm) chemical shifts. Examining more closely at the core of spiro-OMeTAD, the fluorene carbon sites (purple dots) and the fluorene protons are intra- and intermolecularly dipolar coupled, leading to the 2D peaks at ^{13}C (153-155 ppm) and ^{1}H (5.6-7.2 ppm) signals. Right next to it, the phenyl quaternary carbon atoms (denoted by green dots that are adjacent to methoxy groups) are inter- and intramolecularly dipolar coupled to phenyl protons within 3.4 Å distance, leading to the 2D peaks between ^{13}C (158-163 ppm) and ^{1}H (5.5- 7.1 ppm) signals. Apparently, the 2D peaks between ^{13}C (150-160 ppm) and ^{1}H (2-4 ppm) depicted in the box (Figure 5b) indicate the close proximity between quaternary phenyl carbons and the methoxy protons. In this case, large deviations between the experimental and calculated 2D ^{1}H-^{13}C peaks are observed, particularly for the ^{13}C chemical shifts (100-140 ppm) and the methoxy ^{1}H chemical shifts (2-4 ppm) denoted in dashed rectangles, which are expected to originate from through-space dipolar interactions. This indicates that the changes occur in local structures and packing interactions due to different conformational degrees of freedom associated with methoxy groups. A detailed NMR crystallography analysis of 2D

HETCOR spectra of neat spiro-OMeTAD is expected to help to analyze the similar interactions in spiro-OMeTAD:BCF blend, however, the extensive peak broadening and signal intensity losses make it difficult to acquire 2D ^{1}H-^{13}C HETCOR spectra of this latter. We, therefore, acquired and analyzed ^{1}H-^{1}H correlation experiments to examine the morphological changes in the BCF-doped spiro-OMeTAD material, as these experiments benefit from inherently high sensitivity.

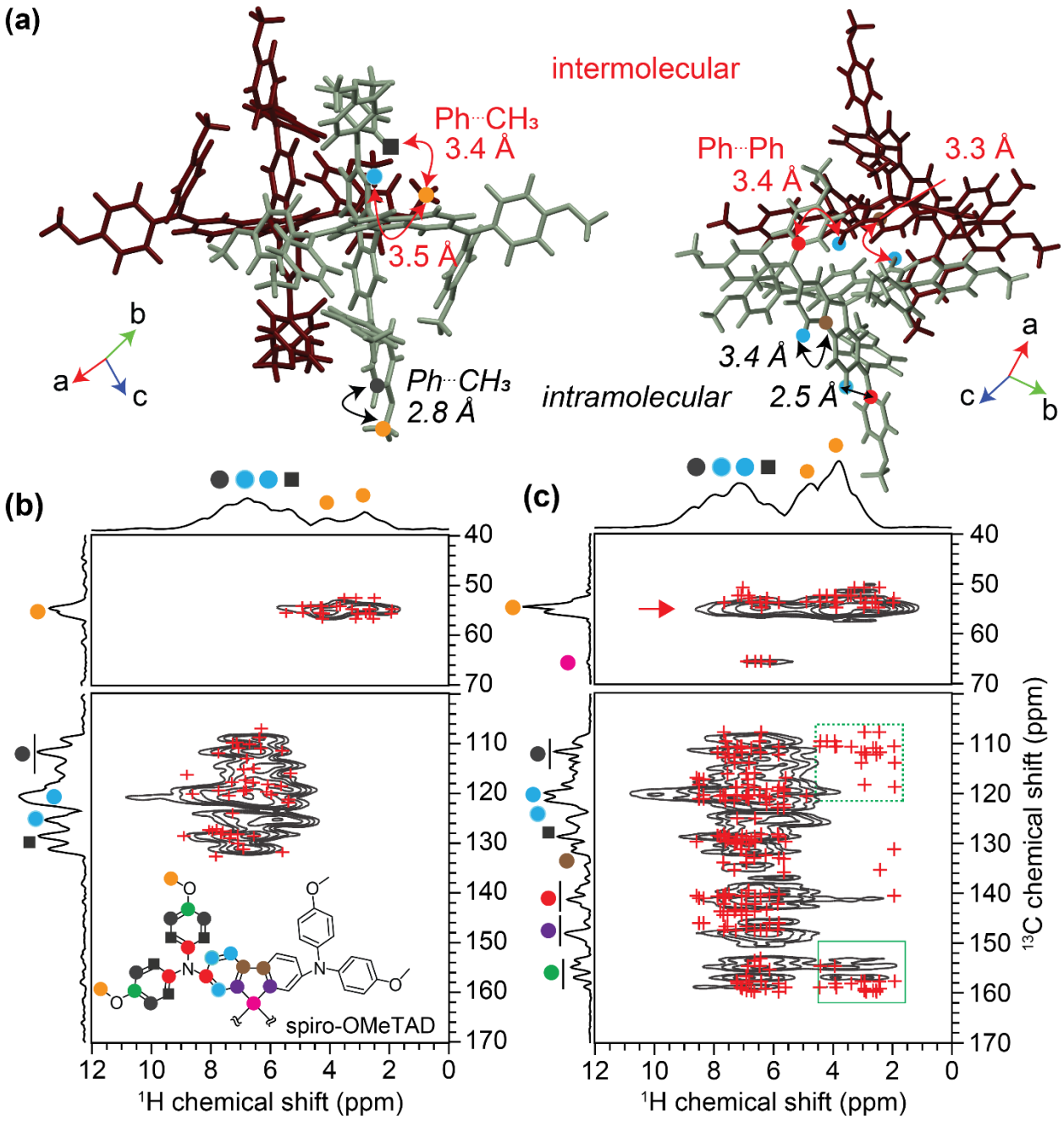

Figure 5. (a) GIPAW DFT-D geometry optimized crystal structure of spiro-OMeTAD with specific inter- and intramolecular packing interactions that contribute to 2D peaks in the ^{1}H-^{13}C HETCOR NMR spectra. Solid-state 2D ^{1}H–^{13}C HETCOR (^{1}H-detected) NMR spectra of spiro-OMeTAD with CP contact time of (b) 100 μs (c) 3 ms along with the skyline projections of ^{1}H and ^{13}C spectra in top-horizontal and left vertical dimensions. DFT calculated NMR chemical shifts of spiro-OMeTAD are overlaid on their spectra. All 2D spectra were acquired at 18.8 T, room temperature, and 50 kHz MAS frequency. For the crystal structures of spiro-OMeTAD, the DFT calculated ^{1}H and ^{13}C chemical shifts for all ^{1}H-^{13}C pairs within (a) 1.3 Å and (b) 2.6 Å is depicted by the overlaid crosses.

Next, we analyzed 2D ^{1}H DQ-SQ correlation spectra of neat spiro-OMeTAD and spiro-OMeTAD:BCF (1:4) blend. In the 2D ^{1}H DQ-SQ correlation experiment, the DQ ^{1}H signals associated with the through-space dipolar coupled ^{1}H-^{1}H pairs within 5 Å are excited and detected. These DQ signals are manifested as on- and off-diagonal correlation peaks at the sum of ^{1}H SQ chemical shifts (see Figure 6, the chemical shift range in the vertical DQ axis is twice as larger as the horizontal SQ chemical shifts), whereby the DQ peak intensities are characteristic to the strength of dipolar interaction between specific ^{1}H-^{1}H pairs.[89–91] Figure 6 presents 2D ^{1}H-^{1}H DQ-SQ correlation spectra of undoped and BCF-doped spiro-OMeTAD blends. For the pristine spiro-OMeTAD material (Figure 6a), the GIPAW DFT-D calculated chemical shifts for all ^{1}H-^{1}H pairs within 2.5 Å are overlaid and compared. A broad distribution of ^{1}H DQ peaks centered at ~3 ppm at the diagonal corresponds to dipolar coupled ^{1}H-^{1}H pairs in methoxy groups, and the distribution of DQ signals at 10-16 ppm is due to the close ^{1}H-^{1}H proximities in aromatic groups. Specifically, the off-diagonal DQ signals at 7.5 and 10.5 ppm (blue arrows) are attributed to the inter- and intramolecular dipolar interactions between methoxy and aromatic groups with the closest ^{1}H-^{1}H distances of 2.5 Å and 2.3 Å, respectively. In contrast to the pristine material, the BCF-doped spiro-OMeTAD exhibits relatively broad DQ-SQ features, which indicates that the addition of BCF molecules causes changes to the local order and intermolecular interactions between spiro-OMeTAD molecules. The relative displacement of the off-diagonal DQ peaks at 9-11 ppm (compared to 7.5-10.5 ppm in neat spiro-OMeTAD) corroborates the changes in the local structures and proximities upon the addition of BCF molecules. For example, the 2D peaks between methoxy and aromatic protons (blue arrows) were not detected in the DQ-SQ spectrum

of spiro-OMeTAD:BCF blend (Figure 6b) due to the changes in the packing interactions of spiro-OMeTAD molecules. In addition, the degree of signal intensity loss in the aromatic regions is higher than the methoxy groups, which further indicates the paramagnetic species are closely located in the aromatic regions. It can be visualized by examining horizontal line-cut spectra of 2D ^{1}H DQ spectra of neat and doped spiro-OMeTAD shown in Figure 6c-d, whereby the on- and off-diagonal ^{1}H DQ signal intensities of the aromatic proton sites in the BCF-doped spiro-OMeTAD is reduced compared to the methoxy groups (in contrast to the nearly identical ^{1}H DQ intensities associated with the same groups in pristine spiro-OMeTAD). Overall, this analysis suggests that the addition of dopant molecules perturb the local structures and packing interactions due to the OSC-dopant miscibility and intermolecular interactions.

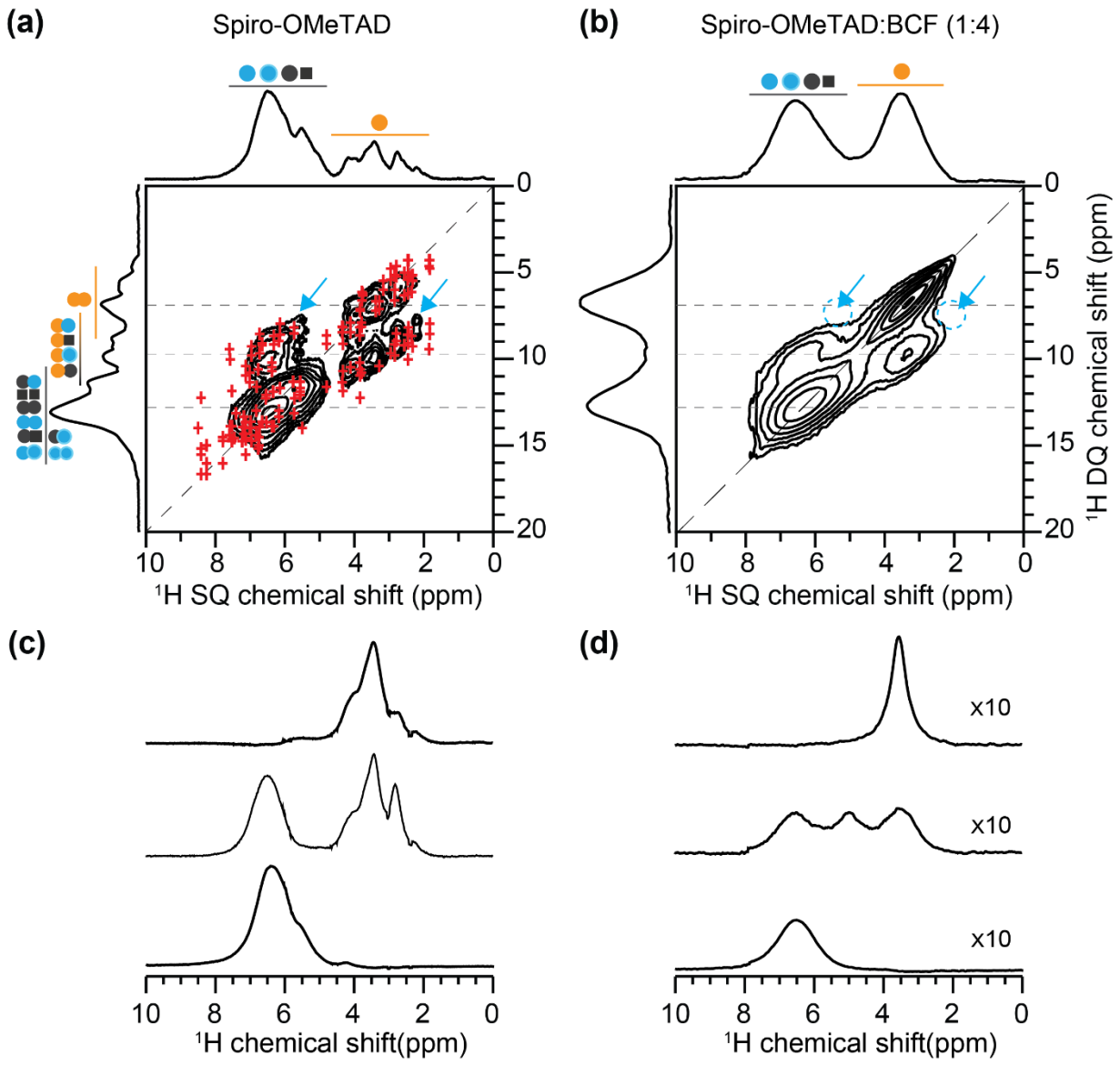

Figure 6. Solid-state ^{1}H-^{1}H DQ-SQ correlation MAS NMR spectra of (a) undoped and (b) BCF-doped spiro-OMeTAD acquired at 18.8 T (^{1}H 800 MHz), 50 kHz MAS and at room temperature. For the undoped spiro-OMeTAD shown in (a), the GIPAW DFT-D calculated chemical shifts for all ^{1}H-^{1}H pairs within 2.5 Å are overlaid on top of the experimental spectrum (blue crosses). The horizontal line-cut spectra of (c) undoped and (d) BCF-doped spiro-OMeTAD molecules are extracted and compared for specific ^{1}H DQ peaks (~7.0, 9.7, and 12.9 ppm) as indicated by the horizontal dashed lines in (a) and (b).

The key learnings from multinuclear (^{1}H, ^{11}B, ^{13}C, and ^{19}F) ssNMR analyses of undoped and doped spiro-OMeTAD are summarized in the following points: (i) Distinct BCF and BCF-water

complexes are identified using 1D ^{11}B NMR analyses (ii) Molecular self-assembly and packing interactions in spiro-OMeTAD are perturbed upon the addition of BCF molecules as observed by the changes in ^{1}H, ^{19}F and ^{13}C NMR chemical shifts and ^{1}H-^{1}H dipolar interactions, and (iii) Significant reduction of signal intensity is observed upon addition of BCF dopant (predominantly for aromatic spiro-OMeTAD moieties) suggesting the formation of paramagnetic species in doped material, which will be corroborated by EPR analysis, as discussed below.

Insight into paramagnetic species and hyperfine interactions by 1D and 2D EPR techniques. Information on the paramagnetic species and hyperfine interactions in doped organic semiconductors can be obtained by analyzing EPR spectra.[52,53,60,92] Figure 7a compares the X-band continuous-wave length (CW) EPR spectra of doped and undoped spiro-OMeTAD films. The undoped spiro-OMeTAD displays a weak intensity signal at a magnetic field centered at 3494 Gauss (G) with a g value of 2.0042 that is characteristic of free-electron g-factor, which is expected to originate from a small concentration of spiro-OMeTAD^{+} cation species generated upon exposure to oxygen.[21,33,93] For spiro-OMeTAD:BCF (1:1 molar ratio), a broad distribution of signals near 3493 G is observed with a g value of 2.0045, and a linewidth of 4.5 G indicate the presence of different paramagnetic species, predictably spiro-OMeTAD^{+} and spiro-OMeTAD-NH•. For example, an electron transfer can occur from the adjacent neutral OSC molecules to the protonated OSC molecules to lead to radical species.[21,48,51,52,94,95] Although the p-type doping leads to spiro-OMeTAD-NH• (with optical absorption at ~620 nm in Figure 1), such species are expected to react with each other to release hydrogen gas and regenerate neutral spiro-OMeTAD.[65] For spiro-OMeTAD:BCF molar ratio 1:4, we observed a further increase in the EPR signal intensity at ~3495 G with a decrease of EPR linewidth to 1.6 G (i.e., homogeneous lineshape) and a g factor of 2.0024 close to the free-electron value. Additionally, longitudinal (T_1) and transverse (T_2) relaxation times of electron spins were measured and compared for the doped materials with 1 and 4 BCF molar equivalents. For the spiro-OMeTAD:BCF (1:1), inhomogeneous T_1 and T_2 values of electrons were found to be 1.2 µs and 60 ns, as measured by the inversion recovery and Hahn-echo experiments. Heterogeneity in the EPR lineshape is in accord with the presence of different radical species along with spiro-OMeTAD^{+}. For the spiro-OMeTAD:BCF (1:4 molar ratio), the EPR lineshape is homogenous and a free induction decay (25 ns) has been acquired with T_{1e} of 500 ns. The different electron spin relaxation times (T_1 and T_2) corroborate that the different paramagnetic (or active radical) species co-exist in p-type doped spiro-OMeTAD:BCF blends,

indicating that the different doping mechanisms, depending on the concentrations of the dopant molecules, consistently with the different doping mechanism suggested in the previous studies.[21,36]

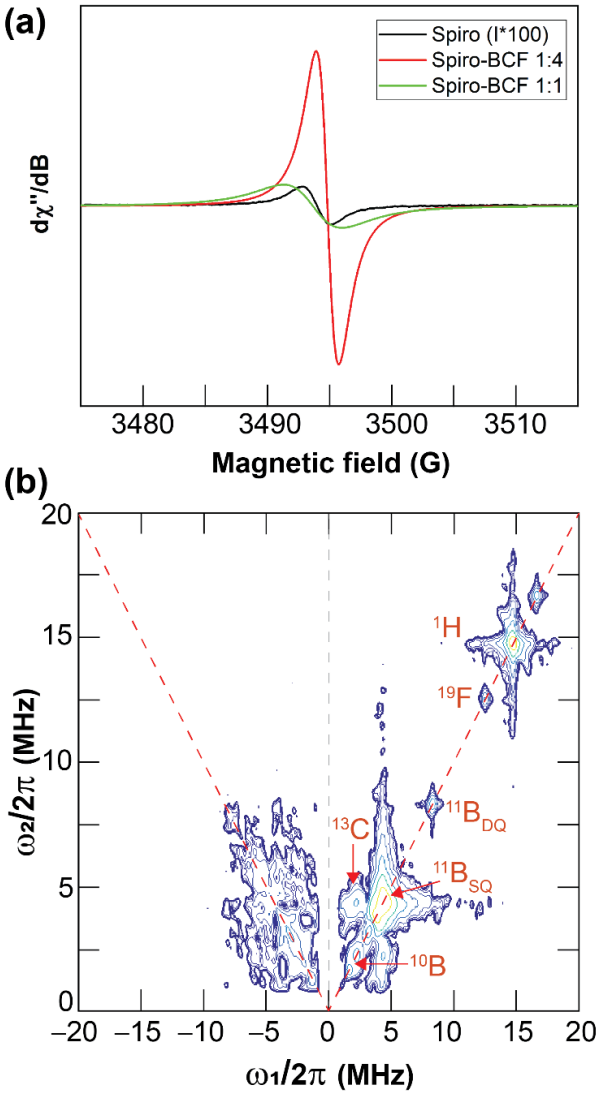

Figure 7. Solid-state (a) CW EPR spectrum for the neat spiro-OMeTAD, and spiro-OMeTAD: BCF blends at 1:1 and 1:4 molar ratios, and (b) 2D HYSCORE spectrum of spiro-OMeTAD: BCF (1:1 molar ratio) acquired at 10 K.

The hyperfine sub-level correlation spectroscopy (HYSCORE) technique is particularly suitable to characterize the hyperfine interactions between electron and nuclear spins in doped OSCs. The HYSCORE spectrum exhibits 2D peaks due to the hyperfine couplings that originate from (i) anisotropic dipole-dipole interaction, which depends on the relative orientation of spin

magnetic moments, and (ii) isotropic fermi-contact interaction that arises when there is a finite spin density of the electron spin at the nucleus. While insight into the local hyperfine interactions in the doped systems can be obtained from pulse 2D EPR techniques, the very fast relaxation times, even at 10 K, makes it difficult to carry out such experiments. Nevertheless, it has been feasible to acquire and analyze the 2D HYSCORE spectrum of spiro-OMeTAD:BCF (1:1) blend (Figure 7b), whereby the hyperfine coupling associated with ^{1}H (~15 MHz) is observed in the (+,+) quadrant of the HYSCORE spectrum.[96,97] A well-resolved ^{19}F at ν=12.5 MHz indicates that the fluorine atoms are spin-polarized by the electrons. The ^{1}H signal at ν=15 MHz indicates a strong electron-proton hyperfine coupling dominated by the dipolar interaction, with a vertical shift of 1.8 MHz indicates an electron-^{1}H distance of ~0.35 nm, suggesting that the bulky aromatic BCF molecules are located in the vicinity of spiro-OMeTAD, as estimated based on the dipole single-point approximation. The same HYSCORE spectrum exhibits weak hyperfine couplings with the two isotopes of boron ^{10}B (ν = 1.6 MHz) and ^{11}B (ν = 4.8 MHz) on the diagonal (red arrows), but does not show an anti-diagonal signal, indicating that these hyperfine interactions arise purely from the dipolar interaction. The broad distributions of signals in the (–,+) quadrant of the same spectrum are expected to originate from the single-quantum and double-quantum signals associated with ^{14}N sites, and weak hyperfine couplings associated with ^{13}C and with ^{14}N sites, which are difficult to resolve and distinguish.

A detailed 2D ssNMR and EPR analyses corroborate that the BCF molecules exhibit different intermolecular interactions with spiro-OMeTAD, which indicate the presence of different oxidized products and radicals that are formed during the p-type doping process. The addition of minuscule concentrations of BCF molecules leads to p-doping of spiro-OMeTAD, which is hypothesized to occur via the Lewis acid-based doping process.[36] Alternative doping process that may occur by transferring the electron from spiro-OMeTAD to BCF molecules, leading to a spiro-OMeTAD radical cation species, cannot be safely ruled out. The positively charged spiro-OMeTAD is hypothesized to be stabilized by the electron transfer from a neighboring neutral spiro-OMeTAD molecule leading to a cation and radical species. In addition, BCF-water complexes serve as Brønsted acid sites to transfer a proton to spiro-OMeTAD molecules, which are hypothesized to trigger p-type doping, particularly at higher concentrations of BCF (greater than 1 molar equivalent),[65] leading to the formation of small amounts of spiro-OMeTAD-H^{+} species as indicated

by changes in the optical absorption (UV-vis spectroscopy) and vibrational spectra (FT-IR spectroscopy) of spiro-OMeTAD:BCF blends .[21]

Conclusions

To summarize, the local compositions, structures and intermolecular interactions in BCF-doped spiro-OMeTAD are investigated using a combination of techniques. Addition of BCF to spiro-OMeTAD yields a strong increase in the optical absorption (400-550 nm), which indicates the formation of oxidized spiro-OMeTAD^{+} species. The spiro-OMeTAD:BCF miscibility and intermolecular interactions are characterized by FT-IR and 1D ^{1}H, ^{13}C, ^{19}F, and ^{11}B MAS NMR, and 2D ^{1}H-^{13}C and ^{1}H-^{1}H correlation NMR spectroscopy techniques. The ^{11}B NMR signals correspond to tri-coordinated BCF, and tetracoordinated BCF anion and BCF-water complexes are distinguished and identified. For pristine spiro-OMeTAD, an NMR crystallography analysis is presented to characterize self-assembly and packing interactions, and this knowledge is extended to rationalize the structural changes in the spiro-OMeTAD films before and after doping with BCF molecules. These results indicate that the BCF molecules are closely associated with spiro-OMeTAD molecules, and cause disruption to the packing interactions of these latter molecules. Specifically, the 2D ^{1}H-^{1}H DQ-SQ correlation NMR spectra enabled the structural changes in undoped and doped materials to be identified and distinguished. In addition, BCF can interact with traces of water molecules to form Brønsted acid BCF-water complexes. These results suggest that the p-type doping by Lewis acid BCF and Brønsted acid BCF-water complexes lead to different dia- and paramagnetic species that are locally distributed into different chemical environments, leading to a mixture of doped and undoped species and aggregates of these molecules. As indicated by ssNMR results, the addition of BCF induces paramagnetic-induced signals broadening and intensity losses. Insight into the hyperfine interactions in BCF-doped spiro-OMeTAD is obtained by analyzing 1D and 2D pulsed EPR techniques and electron spin relaxation measurements and analysis. Despite the amorphous nature of the spiro-OMeTAD thin films, the combined 2D ssNMR and EPR analysis presented here enabled the specific moieties such as aromatic core and methoxy structures and hyperfine interactions to be identified and distinguished. Therefore, the magnetic resonance techniques in conjunction with computational modelling can be applied to obtain essential structural insights and have much wider relevance to characterize intermolecular interactions in small molecule doped organic semiconductors. The presented approach has certain

limitations, as the doped OSCs contain dia- and paramagnetic species that lead to homogeneous and inhomogeneous signal broadening in ssNMR spectra due to the short and long-range effects such as pseudocontact shifts, anisotropic bulk magnetic susceptibility (ABMS)-induced shifts, and the dipolar contributions from the locally disordered regions, which are difficult to accurately deconvolute, analyze and compare.

Author Contributions

Manuscript was written through the contributions of all authors.

Conflicts of interest

There are no conflicts to declare

Acknowledgements

This research is supported by University of Lille and UCCS-UMR-8181 CNRS laboratory. G. N. M. R. acknowledges the support from IR-RMN-THC FR-3050 CNRS France. H. V. acknowledges the support from IR RENARD (FR384). Chevreul Institute (FR CNRS 2638), Ministère de l'Enseignement Supérieur et de la Recherche, Région Nord – Pas de Calais and FEDER are acknowledged for supporting and funding XRD, NMR and EPR facilities. The computational resources were partially provided by the Polish Infrastructure for Supporting Computational Science in the European Research Space (PL-GRID). T.-Q.N. acknowledges the support from the US the US Department of Energy under Award no. DE-SC0017659.

References

(1) Kim, J. Y.; Lee, J. W.; Jung, H. S.; Shin, H.; Park, N. G. High-Efficiency Perovskite Solar Cells. *Chem. Rev.* **2020**, *120*, 7867–7918.

(2) Kunkel, C.; Margraf, J. T.; Chen, K.; Oberhofer, H.; Reuter, K. Active Discovery of Organic Semiconductors. *Nat. Commun.* **2021**, *12*, 2422.

(3) Karki, A.; Gillett, A. J.; Friend, R. H.; Nguyen, T.-Q. The Path to 20% Power Conversion Efficiencies in Nonfullerene Acceptor Organic Solar Cells. *Adv. Energy Mater.* **2021**, *11*, 2003441.

(4) Chen, J.; Xiang, H.; Wang, J.; Wang, R.; Li, Y.; Shan, Q.; Xu, X.; Dong, Y.; Wei, C.; Zeng, H. Perovskite White Light Emitting Diodes: Progress, Challenges, and Opportunities. *ACS Nano* **2021**, *15*, 17150–17174.

(5) Huang, H.; Pradhan, B.; Hofkens, J.; Roeffaers, M. B. J.; Steele, J. A. Solar-Driven Metal Halide Perovskite Photocatalysis: Design, Stability, and Performance. *ACS Energy Lett.* **2020**, *5*, 1107–1123.

(6) Rajagopal, A.; Yao, K.; K-Y Jen, A.; Rajagopal, A.; K-Y Jen, A.; Yao, K. Toward Perovskite Solar Cell Commercialization: A Perspective and Research Roadmap Based on Interfacial Engineering. *Adv. Mater.* **2018**, *30*, 1800455.

(7) Li, Z.; Tinkham, J.; Schulz, P.; Yang, M.; Kim, D. H.; Berry, J.; Sellinger, A.; Zhu, K.; Li, Z.; Schulz, P.; Yang, M.; Kim, D. H.; Berry, J.; Sellinger, A.; Zhu, K.; Tinkham, J. Acid Additives Enhancing the Conductivity of Spiro-OMeTAD Toward High-Efficiency and Hysteresis-Less Planar Perovskite Solar Cells. *Adv. Energy Mater.* **2017**, *7*, 1601451.

(8) Snaith, H. J.; Grätzel, M. Enhanced Charge Mobility in a Molecular Hole Transporter via Addition of Redox Inactive Ionic Dopant: Implication to Dye-Sensitized Solar Cells. *Appl. Phys. Lett.* **2006**, *89*, 262114.

(9) Grancini, G.; Roldán-Carmona, C.; Zimmermann, I.; Mosconi, E.; Lee, X.; Martineau, D.; Narbey, S.; Oswald, F.; De Angelis, F.; Graetzel, M.; Nazeeruddin, M. K. One-Year Stable Perovskite Solar Cells by 2D/3D Interface Engineering. *Nat. Commun.* **2017**, *8*, 15684.

(10) Meng, L.; You, J.; Guo, T. F.; Yang, Y. Recent Advances in the Inverted Planar Structure of Perovskite Solar Cells. *Acc. Chem. Res.* **2015**, *49*, 155–165.

(11) Krishna, A.; Zhang, H.; Zhou, Z.; Gallet, T.; Dankl, M.; Ouellette, O.; Eickemeyer, F. T.; Fu, F.; Sanchez, S.; Mensi, M.; Zakeeruddin, S. M.; Rothlisberger, U.; Manjunatha Reddy, G. N.; Redinger, A.; Grätzel, M.; Hagfeldt, A. Nanoscale Interfacial Engineering Enables Highly Stable and Efficient Perovskite Photovoltaics. *Energy Environ. Sci.* **2021**, *14*, 5552–5562.

(12) Sallenave, X.; Shasti, M.; Anaraki, E. H.; Volyniuk, D.; Grazulevicius, J. V.; Zakeeruddin, S. M.; Mortezaali, A.; Grätzel, M.; Hagfeldt, A.; Sini, G. Interfacial and Bulk Properties of Hole Transporting Materials in Perovskite Solar Cells: Spiro-MeTAD versus Spiro-OMeTAD. *J. Mater. Chem. A* **2020**, *8*, 8527–8539.

(13) Rong, Y.; Hu, Y.; Mei, A.; Tan, H.; Saidaminov, M. I.; Seok, S. Il; McGehee, M. D.; Sargent, E. H.; Han, H. Challenges for Commercializing Perovskite Solar Cells. *Science* **2018**, *361*, eaat8235.

(14) Jeong, J.; Kim, M.; Seo, J.; Lu, H.; Ahlawat, P.; Mishra, A.; Yang, Y.; Hope, M. A.; Eickemeyer, F. T.; Kim, M.; Yoon, Y. J.; Choi, I. W.; Darwich, B. P.; Choi, S. J.; Jo, Y.; Lee, J. H.; Walker, B.; Zakeeruddin, S. M.; Emsley, L.; Rothlisberger, U.; Hagfeldt, A.; Kim, D. S.; Grätzel, M.; Kim, J. Y. Pseudo-Halide Anion Engineering for α-$FAPbI_3$ Perovskite Solar Cells. *Nature* **2021**, *592*, 381–385.

(15) Min, H.; Lee, D. Y.; Kim, J.; Kim, G.; Lee, K. S.; Kim, J.; Paik, M. J.; Kim, Y. K.; Kim, K. S.; Kim, M. G.; Shin, T. J.; Il Seok, S. Perovskite Solar Cells with Atomically Coherent Interlayers on SnO_2 Electrodes. *Nature* **2021**, *598*, 444–450.

(16) Park, B. wook; Kwon, H. W.; Lee, Y.; Lee, D. Y.; Kim, M. G.; Kim, G.; Kim, K. jeong; Kim, Y. K.; Im, J.; Shin, T. J.; Seok, S. Il. Stabilization of Formamidinium Lead Triiodide α-Phase with Isopropylammonium Chloride for Perovskite Solar Cells. *Nat. Energy* **2021**, *6*, 419–428.

(17) Jeong, M.; Choi, I. W.; Go, E. M.; Cho, Y.; Kim, M.; Lee, B.; Jeong, S.; Jo, Y.; Choi, H. W.; Lee, J.; Bae, J. H.; Kwak, S. K.; Kim, D. S.; Yang, C. Stable Perovskite Solar Cells with Efficiency Exceeding 24.8% and 0.3-V Voltage Loss. *Science* **2020**, *369*, 1615–1620.

(18) Dahlman, C. J.; Kubicki, D. J.; Reddy, G. N. M. Interfaces in Metal Halide Perovskites Probed by Solid-State NMR Spectroscopy. *J. Mater. Chem. A* **2021**, *9*, 19206–19244.

(19) Scaccabarozzi, A. D.; Basu, A.; Aniés, F.; Liu, J.; Zapata-Arteaga, O.; Warren, R.; Firdaus, Y.; Nugraha, M. I.; Lin, Y.; Campoy-Quiles, M.; Koch, N.; Müller, C.; Tsetseris, L.; Heeney, M.; Anthopoulos, T. D. Doping Approaches for Organic Semiconductors. *Chem. Rev.* **2022**, *122*, 4420–4492.

(20) Krishna, A.; Grimsdale, A. C. Hole Transporting Materials for Mesoscopic Perovskite Solar Cells – towards a Rational Design? *J. Mater. Chem. A* **2017**, *5*, 16446–16466.

(21) Abate, A.; Hollman, D. J.; Teuscher, J.; Pathak, S.; Avolio, R.; D'Errico, G.; Vitiello, G.; Fantacci, S.; Snaith, H. J. Protic Ionic Liquids as P-Dopant for Organic Hole Transporting Materials and Their Application in High Efficiency Hybrid Solar Cells. *J. Am. Chem. Soc.* **2013**, *135*, 13538–13548.

(22) Li, Y.; Li, H.; Zhong, C.; Sini, G.; Brédas, J. L. Characterization of Intrinsic Hole Transport in Single-Crystal Spiro-OMeTAD. *npj Flex. Electron.* **2017**, *1*, 2.

(23) Shi, D.; Qin, X.; Li, Y.; He, Y.; Zhong, C.; Pan, J.; Dong, H.; Xu, W.; Li, T.; Hu, W.; Brédas, J. L.; Bakr, O. M. Spiro-OMeTAD Single Crystals: Remarkably Enhanced Charge-Carrier Transport via Mesoscale Ordering. *Sci. Adv.* **2016**, *2*, e1501491.

(24) Hu, X.; Wang, H.; Ying, Y.; Wang, M.; Zhang, C.; Ding, Y.; Li, H.; Li, W.; Zhao, S.; Zang, Z. Methylammonium Chloride as an Interface Modificator for Planar-Structure Perovskite Solar Cells with a High Open Circuit Voltage of 1.19V. *J. Power Sources* **2020**, *480*, 229073.

(25) Zhang, C.; Wang, H.; Li, H.; Zhuang, Q.; Gong, C.; Hu, X.; Cai, W.; Zhao, S.; Chen, J.; Zang, Z. Simultaneous Passivation of Bulk and Interface Defects through Synergistic Effect of Anion and Cation toward Efficient and Stable Planar Perovskite Solar Cells. *J. Energy Chem.* **2021**, *63*, 452–460.

(26) Zhuang, Q.; Wang, H.; Zhang, C.; Gong, C.; Li, H.; Chen, J.; Zang, Z. Ion Diffusion-Induced Double Layer Doping toward Stable and Efficient Perovskite Solar Cells. *Nano*

Res. **2022**, 1–9. https://doi.org/10.1007/s12274-022-4135-7.

(27) Yang Michael, Y.; Chen, Q.; Hsieh, Y. T.; Song, T. Bin; Marco, N. De; Zhou, H.; Yang, Y. Multilayer Transparent Top Electrode for Solution Processed Perovskite/Cu(In,Ga)$(Se,S)_2$ Four Terminal Tandem Solar Cells. *ACS Nano* **2015**, *9*, 7714–7721.

(28) Murugan, P.; Ting, H.; Xiaotian, H.; Chen, Y. Advancements in Organic Small Molecule Hole-Transporting Materials for Perovskite Solar Cells: Past and Future. *J. Mater. Chem. A* **2022**, *10*, 5044–5081.

(29) Ren, G.; Han, W.; Deng, Y.; Wu, W.; Li, Z.; Guo, J.; Bao, H.; Liu, C.; Guo, W. Strategies of Modifying Spiro-OMeTAD Materials for Perovskite Solar Cells: A Review. *J. Mater. Chem. A* **2021**, *9*, 4589–4625.

(30) Hawash, Z.; Ono, L. K.; Qi, Y. Moisture and Oxygen Enhance Conductivity of LiTFSI-Doped Spiro-MeOTAD Hole Transport Layer in Perovskite Solar Cells. *Adv. Mater. Interfaces* **2016**, *3*, 1600117.

(31) Schölin, R.; Karlsson, M. H.; Eriksson, S. K.; Siegbahn, H.; Johansson, E. M. J.; Rensmo, H. Energy Level Shifts in Spiro-OMeTAD Molecular Thin Films When Adding Li-TFSI. *J. Phys. Chem. C* **2012**, *116*, 26300–26305.

(32) Kasparavicius, E.; Franckevičius, M.; Malinauskiene, V.; Genevičius, K.; Getautis, V.; Malinauskas, T. Oxidized Spiro-OMeTAD: Investigation of Stability in Contact with Various Perovskite Compositions. *ACS Appl. Energy Mater.* **2021**, *4*, 13696–13705.

(33) Abate, A.; Leijtens, T.; Pathak, S.; Teuscher, J.; Avolio, R.; Errico, M. E.; Kirkpatrik, J.; Ball, J. M.; Docampo, P.; McPherson, I.; Snaith, H. J. Lithium Salts as "Redox Active" p-Type Dopants for Organic Semiconductors and Their Impact in Solid-State Dye-Sensitized Solar Cells. *Phys. Chem. Chem. Phys.* **2013**, *15*, 2572–2579.

(34) Tumen-Ulzii, G.; Matsushima, T.; Adachi, C. Mini-Review on Efficiency and Stability of Perovskite Solar Cells with Spiro-OMeTAD Hole Transport Layer: Recent Progress and Perspectives. *Energy & Fuels* **2021**, *35*, 18915–18927.

(35) Tumen-Ulzii, G.; Qin, C.; Matsushima, T.; Leyden, M. R.; Balijipalli, U.; Klotz, D.; Adachi, C. Understanding the Degradation of Spiro-OMeTAD-Based Perovskite Solar Cells at High Temperature. *Sol. RRL* **2020**, *4*, 2000305.

(36) Ye, T.; Wang, J.; Chen, W.; Yang, Y.; He, D. Improved Performance and Reproducibility of Perovskite Solar Cells by Well-Soluble Tris(Pentafluorophenyl)Borane as a p-Type Dopant. *ACS Appl. Mater. Interfaces* **2017**, *9*, 17923–17931.

(37) Sakai, N.; Warren, R.; Zhang, F.; Nayak, S.; Liu, J.; Kesava, S. V.; Lin, Y.-H.; Biswal, H. S.; Lin, X.; Grovenor, C.; Malinauskas, T.; Basu, A.; Anthopoulos, T. D.; Getautis, V.; Kahn, A.; Riede, M.; Nayak, P. K.; Snaith, H. J. Adduct-Based p-Doping of Organic Semiconductors. *Nat. Mater.* **2021**, *20*, 1248–1254.

(38) Seo, J. Y.; Akin, S.; Zalibera, M.; Preciado, M. A. R.; Kim, H. S.; Zakeeruddin, S. M.; Milić, J. V.; Grätzel, M. Dopant Engineering for Spiro-OMeTAD Hole-Transporting Materials towards Efficient Perovskite Solar Cells. *Adv. Funct. Mater.* **2021**, *31*, 2102124.

(39) Han, Y.; Barnes, G.; Lin, Y. H.; Martin, J.; Al-Hashimi, M.; Alqaradawi, S. Y.; Anthopoulos, T. D.; Heeney, M. Doping of Large Ionization Potential Indenopyrazine Polymers via Lewis Acid Complexation with Tris(Pentafluorophenyl)Borane: A Simple Method for Improving the Performance of Organic Thin-Film Transistors. *Chem. Mater.* **2016**, *28*, 8016–8024.

(40) Zalar, P.; Henson, Z. B.; Welch, G. C.; Bazan, G. C.; Nguyen, T.-Q. Color Tuning in Polymer Light-Emitting Diodes with Lewis Acids. *Angew. Chemie Int. Ed.* **2012**, *51*, 7495–7498.

(41) Pingel, P.; Arvind, M.; Kölln, L.; Steyrleuthner, R.; Kraffert, F.; Behrends, J.; Janietz, S.; Neher Pingel, D. P.; Kölln, L.; Janietz, S.; Arvind, M.; Neher, D.; Steyrleuthner, R.; Kraffert, F.; Behrends, J. P-Type Doping of Poly(3-Hexylthiophene) with the Strong Lewis Acid Tris(Pentafluorophenyl)Borane. *Adv. Electron. Mater.* **2016**, *2*, 1600204.

(42) Welch, G. C.; Coffin, R.; Peet, J.; Bazan, G. C. Band Gap Control in Conjugated Oligomers via Lewis Acids. *J. Am. Chem. Soc.* **2009**, *131*, 10802–10803.

(43) Welch, G. C.; Bazan, G. C. Lewis Acid Adducts of Narrow Band Gap Conjugated Polymers. *J. Am. Chem. Soc.* **2011**, *133*, 4632–4644.

(44) Jia, J.; Dong, J.; Shi, B.; Wu, J.; Wu, Y.; Cao, B. Postpassivation of $Cs_{0.05}(FA_{0.83}MA_{0.17})_{0.95}Pb(I_{0.83}Br_{0.17})_3$ Perovskite Films with Tris(Pentafluorophenyl)Borane. *ACS Appl. Mater. Interfaces* **2021**, *13*, 2472–2482.

(45) Ye, T.; Chen, W.; Jin, S.; Hao, S.; Zhang, X.; Liu, H.; He, D. Enhanced Efficiency of Planar Heterojunction Perovskite Solar Cells by a Light Soaking Treatment on Tris(Pentafluorophenyl)Borane-Doped Poly(Triarylamine) Solution. *ACS Appl. Mater. Interfaces* **2019**, *11*, 14004–14010.

(46) Zalar, P.; Kuik, M.; Henson, Z. B.; Woellner, C.; Zhang, Y.; Sharenko, A.; Bazan, G. C.; Nguyen, T.-Q. Increased Mobility Induced by Addition of a Lewis Acid to a Lewis Basic Conjugated Polymer. *Adv. Mater.* **2014**, *26*, 724–727.

(47) Yurash, B.; Leifert, D.; Reddy, G. N. M.; Cao, D. X.; Biberger, S.; Brus, V. V.; Seifrid, M.; Santiago, P. J.; Köhler, A.; Chmelka, B. F.; Bazan, G. C.; Nguyen, T.-Q. Atomic-Level Insight into the Postsynthesis Band Gap Engineering of a Lewis Base Polymer Using Lewis Acid Tris(Pentafluorophenyl)Borane. *Chem. Mater.* **2019**, *31*, 6715–6725.

(48) Yurash, B.; Cao, D. X.; Brus, V. V.; Leifert, D.; Wang, M.; Dixon, A.; Seifrid, M.; Mansour, A. E.; Lungwitz, D.; Liu, T.; Santiago, P. J.; Graham, K. R.; Koch, N.; Bazan, G. C.; Nguyen, T.-Q. Towards Understanding the Doping Mechanism of Organic Semiconductors by Lewis Acids. *Nat. Mater.* **2019**, *18*, 1327–1334.

(49) Arvind, M.; Tait, C. E.; Guerrini, M.; Krumland, J.; Valencia, A. M.; Cocchi, C.; Mansour, A. E.; Koch, N.; Barlow, S.; Marder, S. R.; Behrends, J.; Neher, D. Quantitative Analysis of Doping-Induced Polarons and Charge-Transfer Complexes of Poly(3-Hexylthiophene) in Solution. *J. Phys. Chem. B* **2020**, *124*, 7694–7708.

(50) Huang, L.; Hu, Z.; Xu, J.; Zhang, K.; Zhang, J.; Zhang, J.; Zhu, Y. Efficient and Stable Planar Perovskite Solar Cells with a Non-Hygroscopic Small Molecule Oxidant Doped Hole Transport Layer. *Electrochim. Acta* **2016**, *196*, 328–336.

(51) Marqués, P. S.; Londi, G.; Yurash, B.; Nguyen, T.-Q.; Barlow, S.; Marder, S. R.; Beljonne, D. Understanding How Lewis Acids Dope Organic Semiconductors: A “Complex” Story. *Chem. Sci.* **2021**, *12*, 7012–7022.

(52) Tait, C. E.; Reckwitz, A.; Arvind, M.; Neher, D.; Bittl, R.; Behrends, J. Spin–Spin Interactions and Spin Delocalisation in a Doped Organic Semiconductor Probed by EPR Spectroscopy. *Phys. Chem. Chem. Phys.* **2021**, *23*, 13827–13841.

(53) Privitera, A.; Warren, R.; Londi, G.; Kaienburg, P.; Liu, J.; Sperlich, A.; Lauritzen, A. E.; Thimm, O.; Ardavan, A.; Beljonne, D.; Riede, M. Electron Spin as Fingerprint for Charge Generation and Transport in Doped Organic Semiconductors. *J. Mater. Chem. C* **2021**, *9*, 2944–2954.

(54) Luginbuhl, B. R.; Raval, P.; Pawlak, T.; Du, Z.; Wang, T.; Schopp, N.; Chae, S.; Yoon, S.; Yi, A.; Kim, H. J.; Coropceanu, V.; Brédas, J.-L.; Nguyen, T.-Q.; Reddy, G. N. M. Resolving Atomic-Scale Interactions in Nonfullerene Acceptor Organic Solar Cells with Solid-State NMR Spectroscopy, Crystallographic Modelling, and Molecular Dynamics Simulations. *Adv. Mater.* **2022**, *34*, 2105943.

(55) Piveteau, L.; Morad, V.; Kovalenko, M. V. Solid-State NMR and NQR Spectroscopy of Lead-Halide Perovskite Materials. *J. Am. Chem. Soc.* **2020**, *142*, 19413–19437.

(56) Kubicki, D. J.; Stranks, S. D.; Grey, C. P.; Emsley, L. NMR Spectroscopy Probes Microstructure, Dynamics and Doping of Metal Halide Perovskites. *Nat. Rev. Chem.* **2021**, *5*, 624–645.

(57) Franssen, W. M. J.; Kentgens, A. P. M. Solid–State NMR of Hybrid Halide Perovskites. *Solid State Nucl. Magn. Reson.* **2019**, *100*, 36–44.

(58) Seifrid, M. T.; Reddy, G. N. M.; Zhou, C.; Chmelka, B. F.; Bazan, G. C. Direct Observation of the Relationship BetweenMolecular Topology and Bulk Morphology for a π-Conjugated Material. *J. Am. Chem. Soc.* **2019**, *141*, 5078–5082.

(59) Raval, P.; Kennard, R. M.; Vasileiadou, E. S.; Dahlman, C. J.; Spanopoulos, I.; Chabinyc,

M. L.; Kanatzidis, M.; Reddy, G. N. M. Understanding Instability in Formamidinium Lead Halide Perovskites: Kinetics of Transformative Reactions at Grain and Subgrain Boundaries. *ACS Energy Lett.* **2022**, *7*, 1534–1543.

(60) Dixon, A. L.; Vezin, H.; Nguyen, T.-Q.; Reddy, G. N. M. Structural Insights into Lewis Acid- and F4TCNQ-Doped Conjugated Polymers by Solid-State Magnetic Resonance Spectroscopy. *Mater. Horizons* **2022**, *9*, 981–990.

(61) Harris, R. K.; Becker, E. D.; Cabral De Menezes, S. M.; Goodfellow, R.; Granger, P. NMR Nomenclature. Nuclear Spin Properties and Conventions for Chemical Shifts (IUPAC Recommendations 2001). *Pure Appl. Chem.* **2001**, *73*, 1795–1818.

(62) Saalwächter, K.; Lange, F.; Matyjaszewski, K.; Huang, C. F.; Graf, R. BaBa-Xy16: Robust and Broadband Homonuclear DQ Recoupling for Applications in Rigid and Soft Solids up to the Highest MAS Frequencies. *J. Magn. Reson.* **2011**, *212*, 204–215.

(63) Manjunatha Reddy, G. N.; Malon, M.; Marsh, A.; Nishiyama, Y.; Brown, S. P. Fast Magic-Angle Spinning Three-Dimensional Nmr Experiment for Simultaneously Probing H–H and N–H Proximities in Solids. *Anal. Chem.* **2016**, *88*, 11412–11419.

(64) Danopoulos, A. A.; Galsworthy, J. R.; Green, M. L. H.; Cafferkey, S.; Doerrer, L. H.; Hursthouse, M. B. Equilibria in the $B(C_6F_5)_3$–H_2O System: Synthesis and Crystal Structures of $H_2O{\cdot}B(C_6F_5)_3$ and the Anions $[HOB(C_6F_5)_3]^-$ and $[(F_5C_6)_3B(\mu\text{-}OH)B(C_6F_5)_3]^-$. *Chem. Commun.* **1998**, 2529–2560.

(65) Doerrer, L. H.; Green, M. L. H. Oxidation of $[M(\eta\text{-}C_5H_5)_2]$, M=Cr, Fe or Co, by the New Brønsted Acid $H_2OB(C_6F_5)_3$ Yielding the Salts $[M(\eta\text{-}C_5H_5)_2]^+A^-$, Where A^- $[(C_6F_5)_3\ B(\mu\text{-}OH)B(C_6F_5)_3]$ or $[(C_6F_5)_3BOH\ldots H_2OB(C_6F_5)_3]$. *J. Chem. Soc. Dalt. Trans.* **1999**, 4325–4329.

(66) Pickard, C. J.; Mauri, F. All-Electron Magnetic Response with Pseudopotentials: NMR Chemical Shifts. *Phys. Rev. B* **2001**, *63*, 245101.

(67) Clark, S. J.; Segall, M. D.; Pickard, C. J.; Hasnip, P. J.; Probert, M. I. J.; Refson, K.; Payne,

M. C. First Principles Methods Using CASTEP. *Zeitschrift fur Krist.* **2005**, *220*, 567–570.

(68) Perdew, J. P.; Burke, K.; Ernzerhof, M. Generalized Gradient Approximation Made Simple. *Phys. Rev. Lett.* **1996**, *77*, 3865.

(69) Tkatchenko, A.; Scheffler, M. Accurate Molecular van Der Waals Interactions from Ground-State Electron Density and Free-Atom Reference Data. *Phys. Rev. Lett.* **2009**, *102*, 073005.

(70) Vanderbilt, D. Soft Self-Consistent Pseudopotentials in a Generalized Eigenvalue Formalism. *Phys. Rev. B* **1990**, *41*, 7892.

(71) Nocedal, J.; S.J.Wright. *Numerical Optimization*; Springer New York, 2006.

(72) Monkhorst, H. J.; Pack, J. D. Special Points for Brillouin-Zone Integrations. *Phys. Rev. B* **1976**, *13*, 5188.

(73) Sturniolo, S.; Green, T. F. G.; Hanson, R. M.; Zilka, M.; Refson, K.; Hodgkinson, P.; Brown, S. P.; Yates, J. R. Visualization and Processing of Computed Solid-State NMR Parameters: MagresView and MagresPython. *Solid State Nucl. Magn. Reson.* **2016**, *78*, 64–70.

(74) Liu, J.; Liu, W.; Aydin, E.; Harrison, G. T.; Isikgor, F. H.; Yang, X.; Subbiah, A. S.; De Wolf, S. Lewis-Acid Doping of Triphenylamine-Based Hole Transport Materials Improves the Performance and Stability of Perovskite Solar Cells. *ACS Appl. Mater. Interfaces* **2020**, *12*, 23874–23884.

(75) Romanos, J.; Beckner, M.; Stalla, D.; Tekeei, A.; Suppes, G.; Jalisatgi, S.; Lee, M.; Hawthorne, F.; Robertson, J. D.; Firlej, L.; Kuchta, B.; Wexler, C.; Yu, P.; Pfeifer, P. Infrared Study of Boron-Carbon Chemical Bonds in Boron-Doped Activated Carbon. *Carbon N. Y.* **2012**, *54*, 208–214.

(76) Karakaş Sarıkaya, E.; Dereli, Ö. Molecular Structure and Vibrational Spectra of 7-Methoxy-4-Methylcoumarin by Density Functional Method. *J. Mol. Struct.* **2013**, *1052*, 214–220.

(77) Ramasamy, R. FTIR and FT-RAMAN Spectral Investigation of Fluorobenzene. *Int. J. Phys. Appl.* **2014**, *6*, 1–6.

(78) Gunasekaran, S.; Seshadri, S.; Muthu, & S. Vibrational Spectra and Normal Coordinate Analysis of Flucytosine. *Indian J. Pure Appl. Phys.* **2006**, *44*, 581–586.

(79) Wang, J.; Li, J.; Xu, X.; Bi, Z.; Xu, G.; Shen, H. Promising Photovoltaic Application of Multi-Walled Carbon Nanotubes in Perovskites Solar Cells for Retarding Recombination. *RSC Adv.* **2016**, *6*, 42413–42420.

(80) Kallol, C.; Wei-Chih, C.; Paul, A. B.; Vineeth, M. V.; Chen, C. C.; Shane, A. C. Superhard Boron-Rich Boron Carbide with Controlled Degree of Crystallinity. *Materials* **2020**, *13*, 3622.

(81) Seifrid, M.; Reddy, G. N. M.; Chmelka, B. F.; Bazan, G. C. Insight into the Structures and Dynamics of Organic Semiconductors through Solid-State NMR Spectroscopy. *Nat. Rev. Mater.* **2020**, *5*, 910–930.

(82) Hansen, M. R.; Graf, R.; Spiess, H. W. Interplay of Structure and Dynamics in Functional Macromolecular and Supramolecular Systems As Revealed by Magnetic Resonance Spectroscopy. *Chem. Rev.* **2016**, *116*, 1272–1308.

(83) Miller, N. C.; Cho, E.; Junk, M. J. N.; Gysel, R.; Risko, C.; Kim, D.; Sweetnam, S.; Miller, C. E.; Richter, L. J.; Kline, R. J.; Heeney, M.; McCulloch, I.; Amassian, A.; Acevedo-Feliz, D.; Knox, C.; Hansen, M. R.; Dudenko, D.; Chmelka, B. F.; Toney, M. F.; Brédas, J. L.; McGehee, M. D. Use of X-Ray Diffraction, Molecular Simulations, and Spectroscopy to Determine the Molecular Packing in a Polymer-Fullerene Bimolecular Crystal. *Adv. Mater.* **2012**, *24*, 6071–6079.

(84) Chaudhari, S. R.; Griffin, J. M.; Broch, K.; Lesage, A.; Lemaur, V.; Dudenko, D.; Olivier, Y.; Sirringhaus, H.; Emsley, L.; Grey, C. P. Donor–Acceptor Stacking Arrangements in Bulk and Thin-Film High-Mobility Conjugated Polymers Characterized Using Molecular Modelling and MAS and Surface-Enhanced Solid-State NMR Spectroscopy. *Chem. Sci.* **2017**, *8*, 3126–3136.

(85) Dudenko, D.; Kiersnowski, A.; Shu, J.; Pisula, W.; Sebastiani, D.; Spiess, H. W.; Hansen, M. R. A Strategy for Revealing the Packing in Semicrystalline π-Conjugated Polymers: Crystal Structure of Bulk Poly-3-Hexyl-Thiophene (P3HT). *Angew. Chemie Int. Ed.* **2012**, *51*, 11068–11072.

(86) Tsao, H. N.; Cho, D. M.; Park, I.; Hansen, M. R.; Mavrinskiy, A.; Yoon, D. Y.; Graf, R.; Pisula, W.; Spiess, H. W.; Müllen, K. Ultrahigh Mobility in Polymer Field-Effect Transistors by Design. *J. Am. Chem. Soc.* **2011**, *133*, 2605–2612.

(87) Karki, A.; H Wetzelaer, G.-J. A.; Reddy, G. N. M.; Nádaždy, V.; Seifrid, M.; Schauer, F.; Bazan, G. C.; Chmelka, B. F.; M Blom, P. W.; Nguyen, T.-Q. Unifying Energetic Disorder from Charge Transport and Band Bending in Organic Semiconductors. *Adv. Funct. Mater.* **2019**, *29*, 1901109.

(88) Samanta, S.; Raval, P.; Reddy, G. N. M.; Chaudhuri, D. Cooperative Self-Assembly Driven by Multiple Noncovalent Interactions: Investigating Molecular Origin and Reassessing Characterization. *ACS Cent. Sci.* **2021**, *7*, 1391–1399.

(89) Brown, S. P. Applications of High-Resolution 1H Solid-State NMR. *Solid State Nucl. Magn. Reson.* **2012**, *41*, 1–27.

(90) Brown, S. P.; Spiess, H. W. Advanced Solid-State NMR Methods for the Elucidation of Structure and Dynamics of Molecular, Macromolecular, and Supramolecular Systems. *Chem. Rev.* **2001**, *101*, 4125–4155.

(91) Brown, S. P. Probing Proton–Proton Proximities in the Solid State. *Prog. Nucl. Magn. Reson. Spectrosc.* **2007**, *50*, 199–251.

(92) Biskup, T. Structure-Function Relationship of Organic Semiconductors: Detailed Insights from Time-Resolved EPR Spectroscopy. *Front. Chem.* **2019**, *7*, 10.

(93) Fantacci, S.; De Angelis, F.; Nazeeruddin, M. K.; Grätzel, M. Electronic and Optical Properties of the Spiro-MeOTAD Hole Conductor in Its Neutral and Oxidized Forms: A DFT/TDDFT Investigation. *J. Phys. Chem. C* **2011**, *115*, 23126–23133.

(94) Alvarez, F. J. D.; Orelle, C.; Davidson, A. L. Functional Reconstitution of an ABC Transporter in Nanodiscs for Use in Electron Paramagnetic Resonance Spectroscopy. *J. Am. Chem. Soc.* **2010**, *132*, 9513–9515.

(95) Goez, M.; Frisch, I.; Sartorius, I. Electron and Hydrogen Self-Exchange of Free Radicals of Sterically Hindered Tertiary Aliphatic Amines Investigated by Photo-CIDNP. *Beilstein J. Org. Chem.* **2013**, *9*, 437–446.

(96) Pöppl, A.; Kevan, L. A Practical Strategy for Determination of Proton Hyperfine Interaction Parameters in Paramagnetic Transition Metal Ion Complexes by Two-Dimensional HYSCORE Electron Spin Resonance Spectroscopy in Disordered Systems. *J. Phys. Chem.* **1996**, *100*, 3387–3394.

(97) McCracken, J.; Casey, T. M.; Hausinger, R. P. ^{1}H-HYSCORE Reveals Structural Details at the Fe(II) Active Site of Taurine:2-Oxoglutarate Dioxygenase. *Appl. Magn. Reson.* **2021**, *52*, 971–994.

Supplementary Information for

Understanding the p-doping of spiro-OMeTAD by tris(pentafluorophenyl)borane

Parth Raval,[1] Margot Dhennin,[1] Hervé Vezin,[2] Tomasz Pawlak,[3] Pascal Roussel,[1] Thuc-Quyen Nguyen,[4] and G. N. Manjunatha Reddy[1*]

[1]*University of Lille, CNRS, Centrale Lille Institut, Univ. Artois, UMR 8181−UCCS− Unité de Catalyse et Chimie du Solide, F-59000, Lille, France*

[2] *University of Lille, CNRS UMR8516, LASIRE, F-59000, Lille, France*

[3]*Centre of Molecular and Macromolecular Studies, Polish Academy of Sciences, Sienkiewicza 112, Lodz 90-363, Poland*

[4] *Center for Polymers and Organic Solids, University of California Santa Barbara (UCSB), Santa Barbara, California 93106, USA*

E-mail: gnm.reddy@univ-lille.fr

Table of contents

1. UV-Vis spectrum of neat and BCF doped spiro-OMeTAD (1:1 and 1:4)

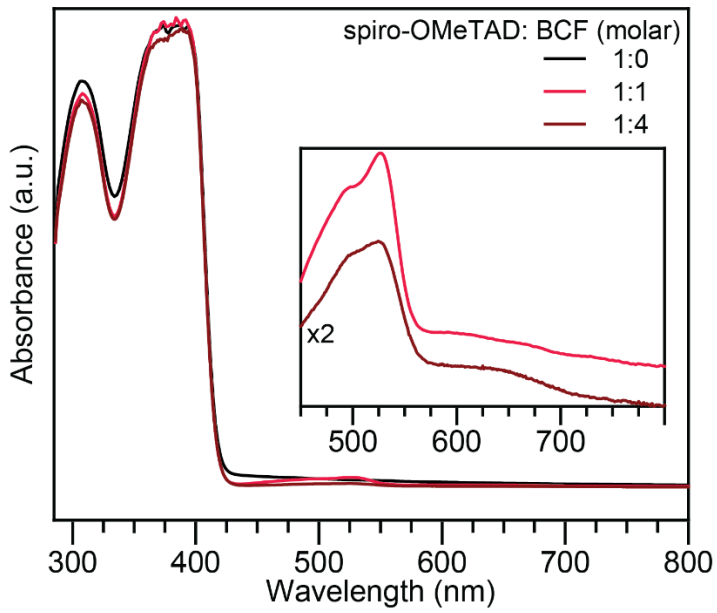

Figure S1. UV-Vis spectra of pristine and BCF-doped spiro-OMeTAD as a function of dopant concentration.

2. Powder X-ray diffraction patterns of neat and doped spiro-OMeTAD

For neat spiro-OMeTAD and BCF-doped spiro-OMeTAD films drop cast on indium tin oxide (ITO)-coated glass substrates, powder XRD patterns are compared in **Figure S2**. Given the amorphous nature of drop cast spiro-OMeTAD film, a strong background signal is observed in the powder XRD pattern, and the reflections at (200), (222), and (400) originating from the ITO glass substrate are detected. By comparison, the spiro-OMeTAD:BCF (1:1 and 1:4 molar ratios) blends exhibited a broad distribution of scattered intensities centered at ~18°, corresponding to the *d*-spacing value of 0.45 nm, which are expected to originate from very weak π–π stacking interactions between BCF and Spiro-OMeTAD molecules. The subtle change in the long-range order observed by XRD indicates changes in spiro-OMeTAD thin-film morphology upon the addition of BCF molecules. Due to the heterogeneous nature of OSCs, obtaining a deeper molecular-level understanding using long-range probes such as X-ray diffraction is, however, challenging; more atomic-level probes are required to provide information on the changes in local structures upon the addition of BCF molecules to the spiro-OMeTAD.

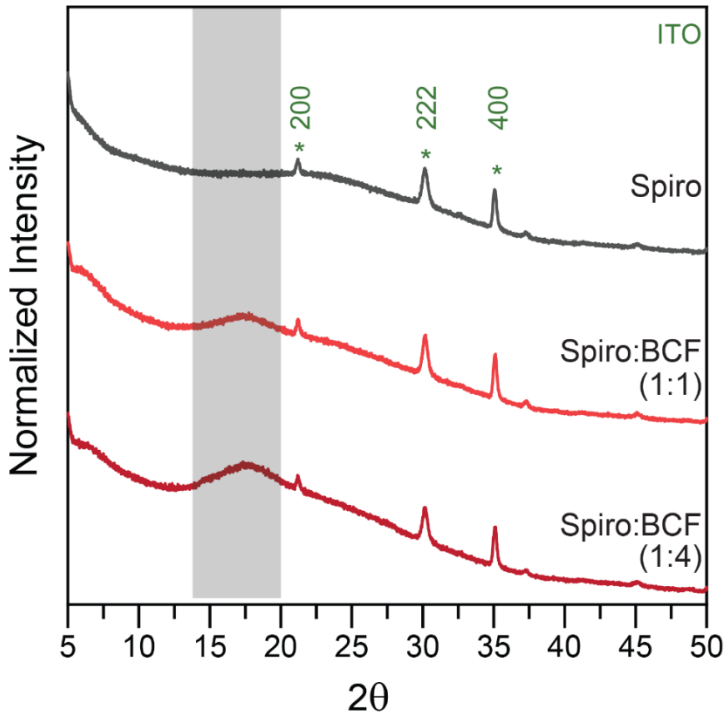

Figure S2. Powder XRD patterns of pristine undoped and doped spiro-OMeTAD thin films drop cast on ITO-coated glass substrates.

3. ^{11}B MAS NMR spectra of spiro-OMeTAD:BCF blends

Figure S3 presents the 1D ^{11}B MAS NMR spectra of spiro-OMeTAD:BCF (1:0.25 and 1:0.5 molar ratio) blends. The peak at −5 ppm in these spectra can be attributed to tetrahedral boron sites in BCF anions. The additional signal around 1 ppm and ~15 ppm in the spiro-OMeTAD:BCF blends (1:0.5 molar ratio) can be attributed to the BCF-water complexes.

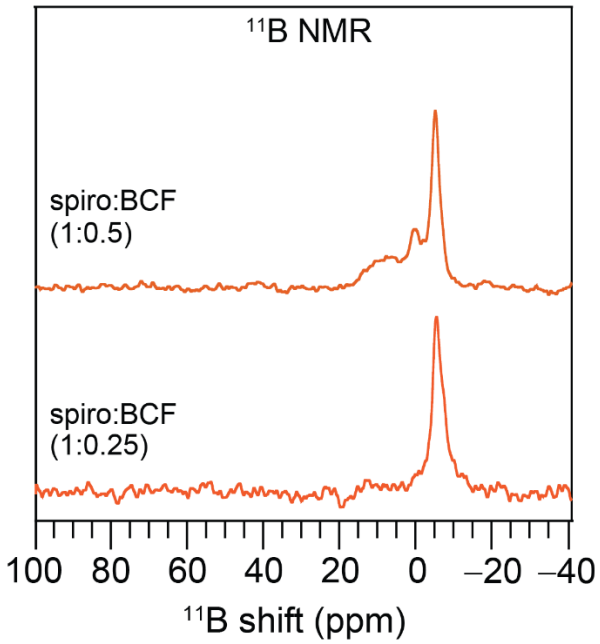

Figure S3. Solid-state ^{11}B MAS NMR spectra of spiro-OMeTAD:BCF blends (1:0.25 and 1:0.5 molar ratio) acquired at 9.4 T (^{11}B Larmor frequency = 128.4 MHz) with 30 kHz MAS at room temperature.

4. ^{1}H MAS NMR spectra of spiro-OMeTAD:BCF blends

Figure S4 presents the 1D ^{1}H MAS NMR spectra of spiro-OMeTAD:BCF (1:0.25 and 1:0.5 molar ratio) blends. The broad peak centered at 3.1 and 6.4 ppm in these spectra can be attributed to methoxy and aromatic protons in the spiro-OMeTAD material. Acquisition of the spectrum at 30 kHz, as well as the presence of anisotropic bulk magnetic susceptibility effects and local disorder, leads to the signal broadening, making it complex to resolve distinct sites in the spiro-OMeTAD:BCF blends.

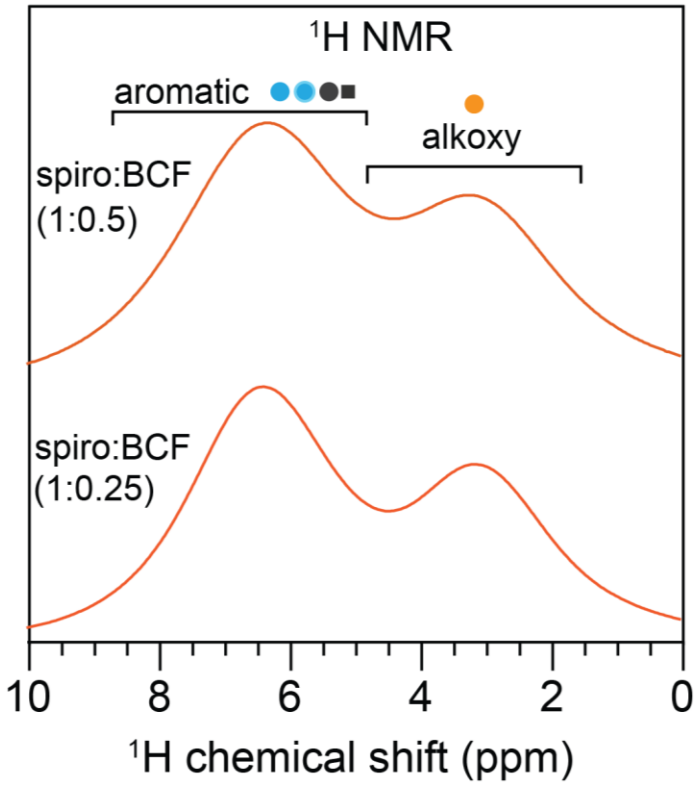

Figure S4. Solid-state ^{1}H MAS NMR spectra of spiro-OMeTAD:BCF blends (1:0.25 and 1:0.5 molar ratio) acquired at 9.4 T (^{1}H Larmor frequency = 400.1 MHz) with 30 kHz MAS. The peaks are color-coded, as depicted in the schematic structure in Figure 4d (main manuscript).

5. ^{19}F MAS NMR spectra of spiro-OMeTAD:BCF blends

Insights into the local chemical environments and structures of pentafluorophenyl groups in neat BCF and spiro-OMeTAD:BCF blends can be obtained by analyzing and comparing their ^{19}F MAS NMR. **Figure S5** presents the 1D ^{19}F MAS NMR spectra of spiro-OMeTAD:BCF (1:0.25 and 1:0.5 molar ratio) blends. In the 1D ^{19}F NMR of neat BCF shown in (Figure 4c, main manuscript), the signals at −134, −138, and −141 ppm correspond to inequivalent *ortho*- fluorine sites in pentafluoro phenyl moieties, and the signals corresponding to the *meta*- and *para*- fluorine sites are observed in the range between −160 and −171 ppm. In the 1D ^{19}F NMR spectrum of spiro-OMeTAD:BCF (1:0.25 and 1:0.5) blends shown in Figure S5, significant line broadening is observed for *ortho*-, *meta*- and *para*- fluorine sites. Upon increasing the dopant concentration, ^{19}F NMR of spiro-OMeTAD:BCF blend (1:1 molar ratio) exhibited a broad signal centered at −134 and −165 ppm. Signal broadening in this material indicates the local compositional and structural disorder and the presence of hyperfine interactions. Upon further increasing the BCF concentration, the ^{19}F signals corresponding to ortho- para- and meta- fluorine sites are observed at −138, −155, and −162 ppm in the spiro-OMeTAD:BCF blend (1:4 molar ratio) material. These signals, in comparison to the 1:1 molar ratio blend, are narrower, suggesting a more locally ordered environment, which can be hypothesized to be originated from the clusters of BCF-water complexes. One must also take into account the anisotropic bulk magnetic susceptibility effects, which further cause signal broadening in spiro-OMeTAD:BCF blends in comparison to pristine BCF material.

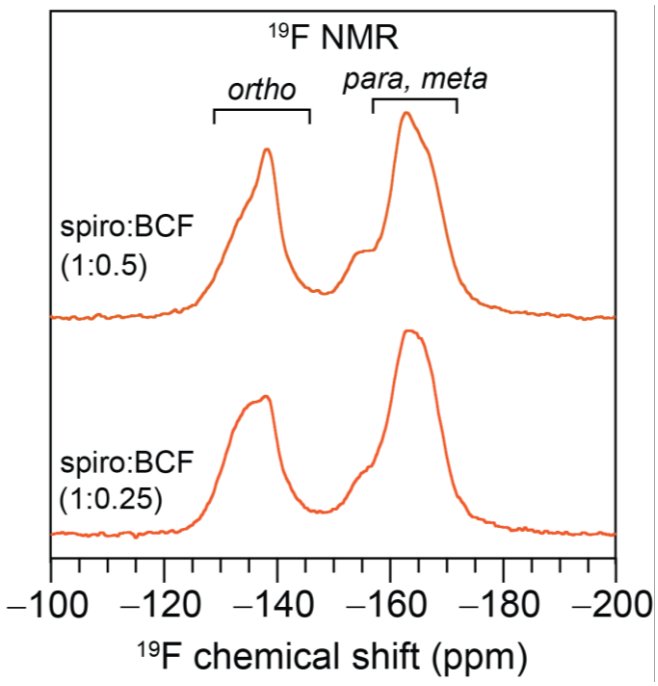

Figure S5. Solid-state ^{19}F MAS NMR spectra of spiro-OMeTAD:BCF blends (1:0.25 and 1:0.5 molar ratio) acquired at 9.4 T (^{19}F Larmor frequency = 376.5 MHz) with 30 kHz MAS.